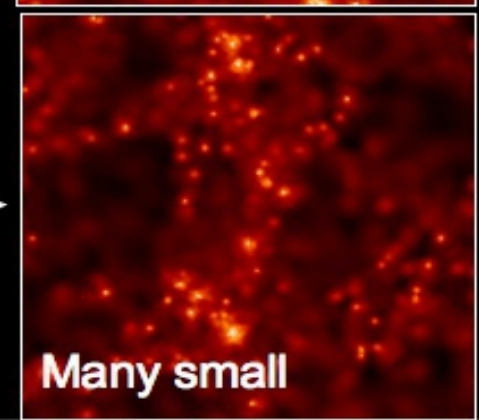
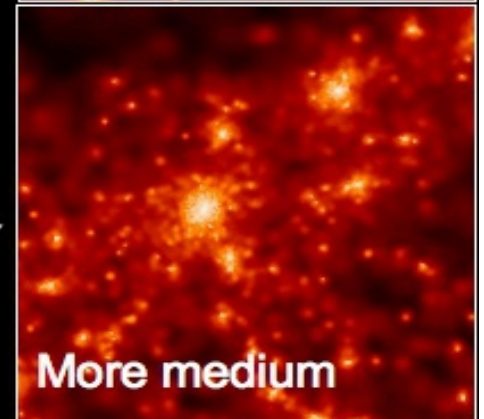
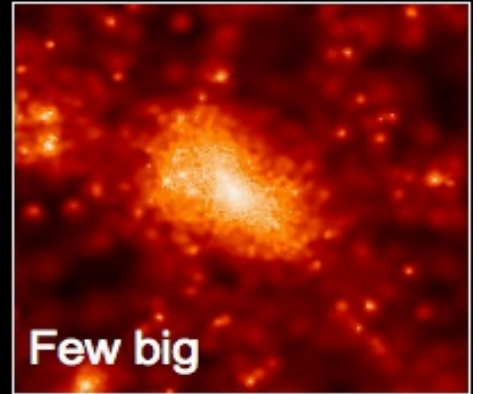
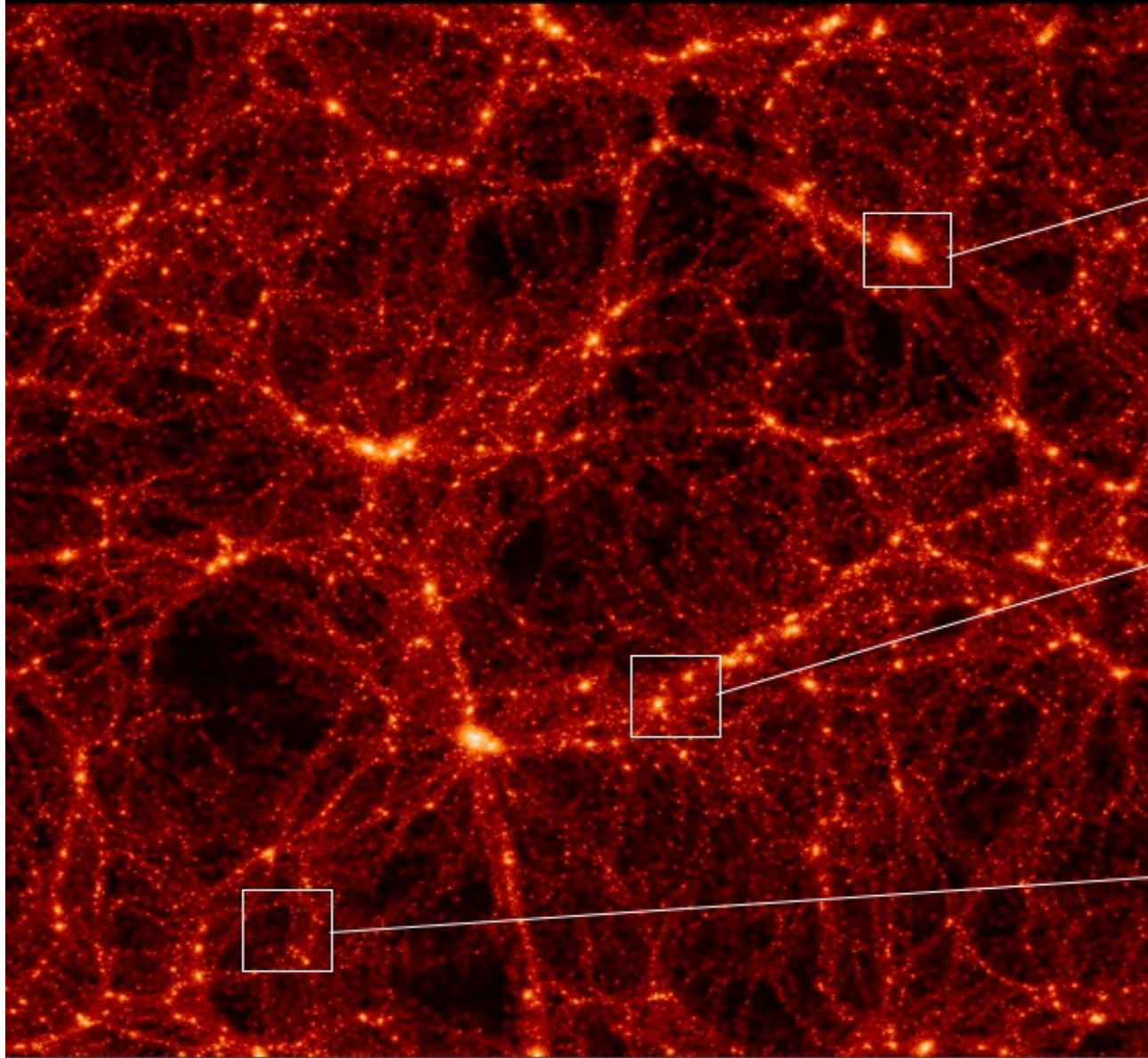
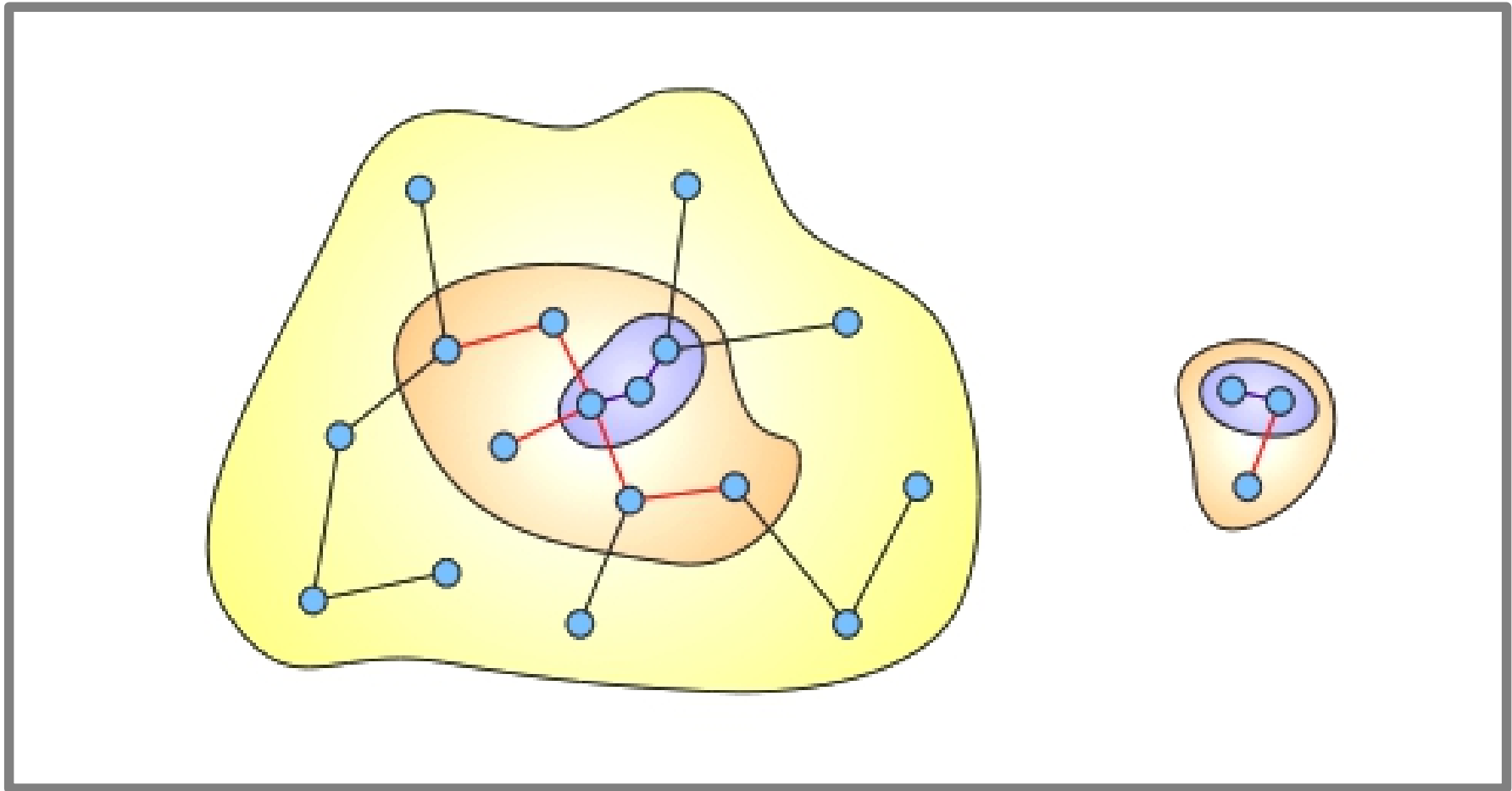


Analysis of Dark Matter Simulations

The Web of Dark Matter Halos





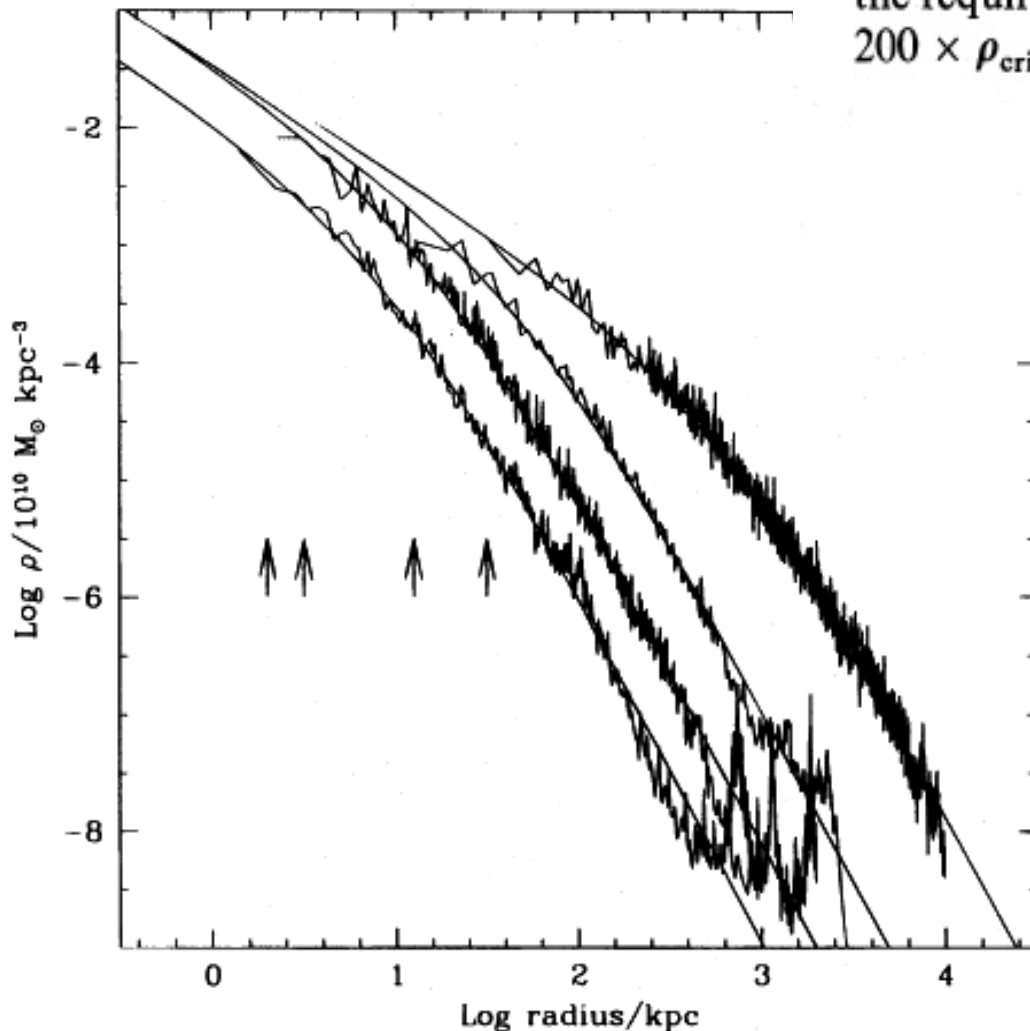
“Friends-of-friends” algorithm for identifying halos at fixed overdensity compared to the mean inter-particle separation.

Navarro, Frenk & White 1996

$$\frac{\rho(r)}{\rho_{\text{crit}}} = \frac{\delta_c}{(r/r_s)(1 + r/r_s)^2}, \quad (3)$$

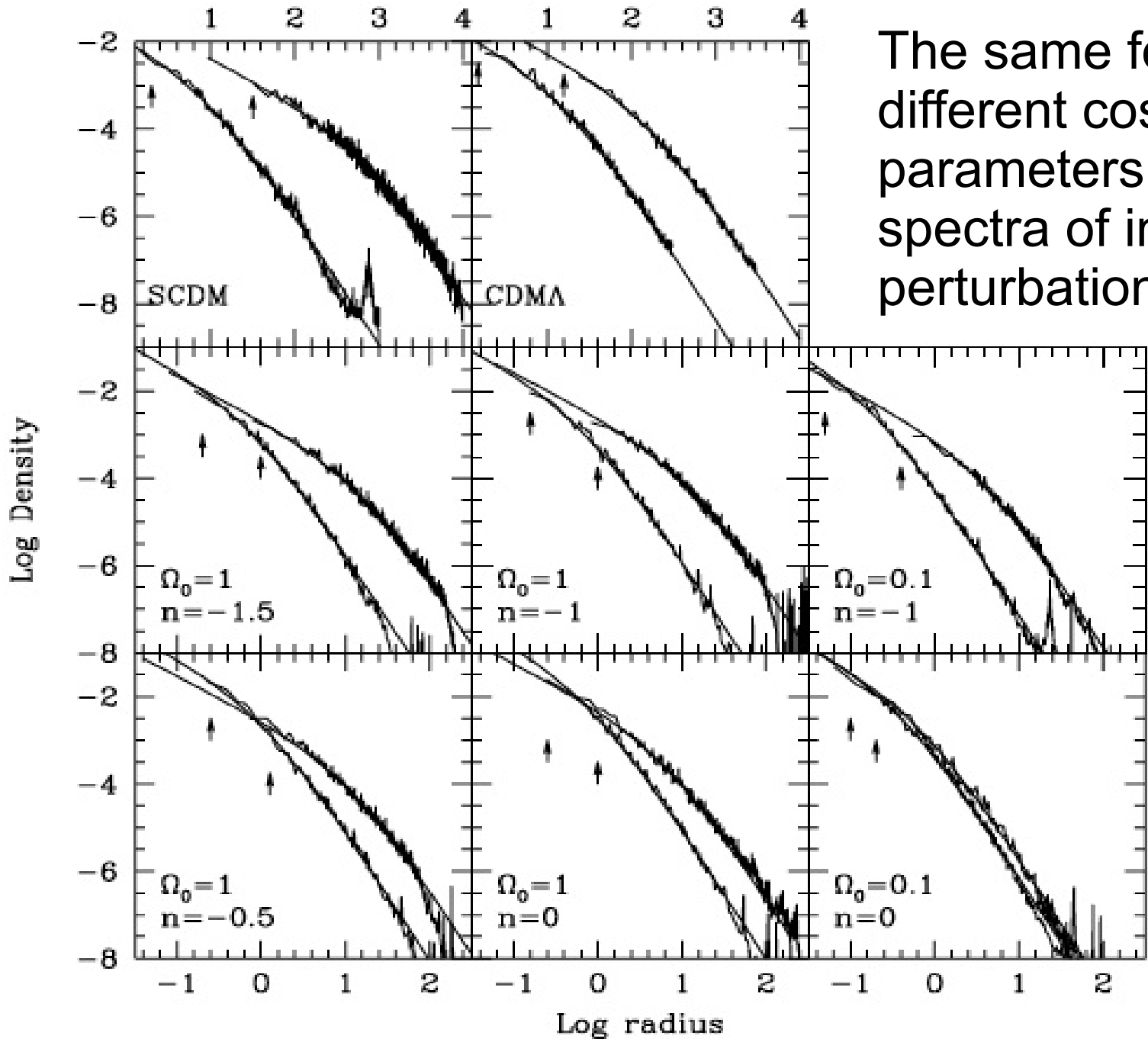
where $r_s = r_{200}/c$ is a characteristic radius and $\rho_{\text{crit}} = 3H^2/8\pi G$ is the critical density (H is the current value of Hubble's constant); δ_c and c are two dimensionless parameters. Note that r_{200} determines the mass of the halo, $M_{200} = 200\rho_{\text{crit}}(4\pi/3)r_{200}^3$, and that δ_c and c are linked by the requirement that the mean density within r_{200} should be $200 \times \rho_{\text{crit}}$. That is,

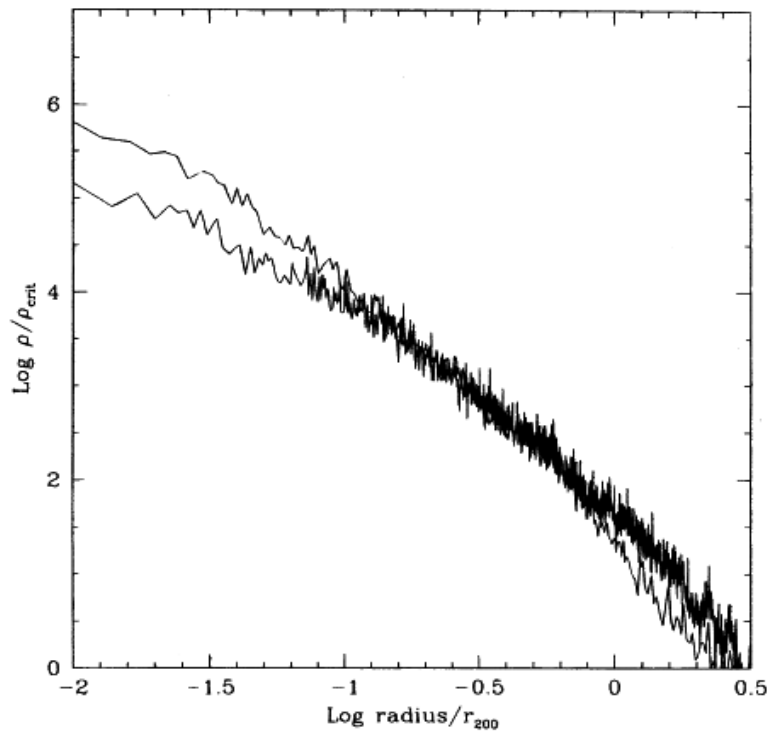
$$\delta_c = \frac{200}{3} \frac{c^3}{[\ln(1+c) - c/(1+c)]}. \quad (4)$$



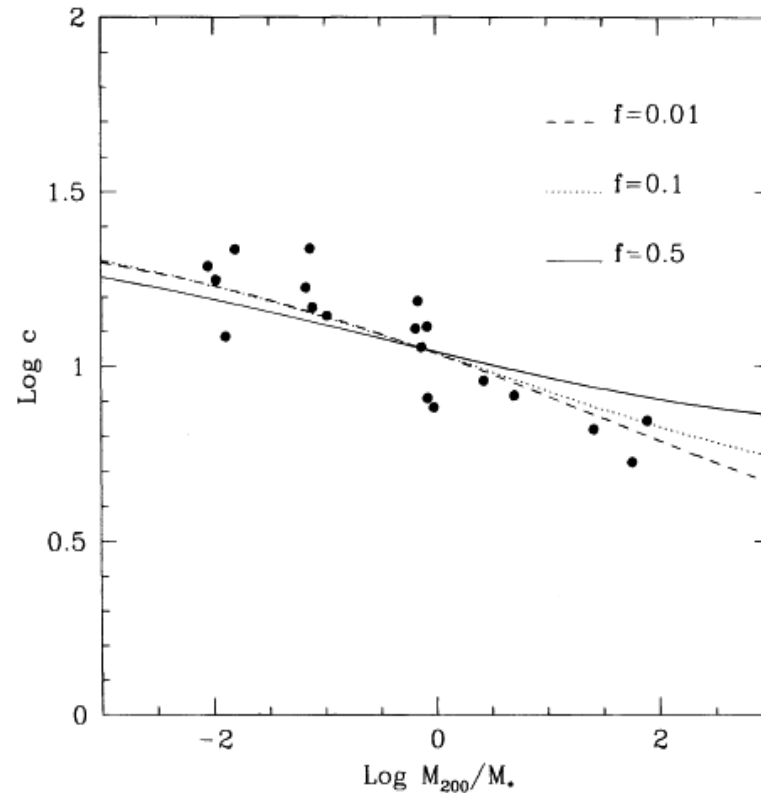
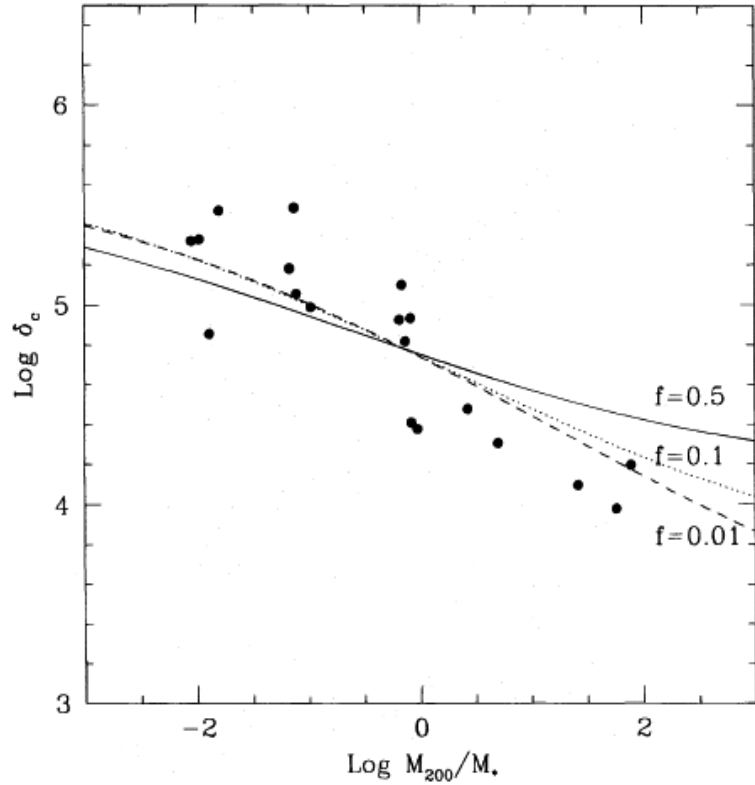
The Density Profiles of Dark Matter Halos Exhibit a “Universal” form

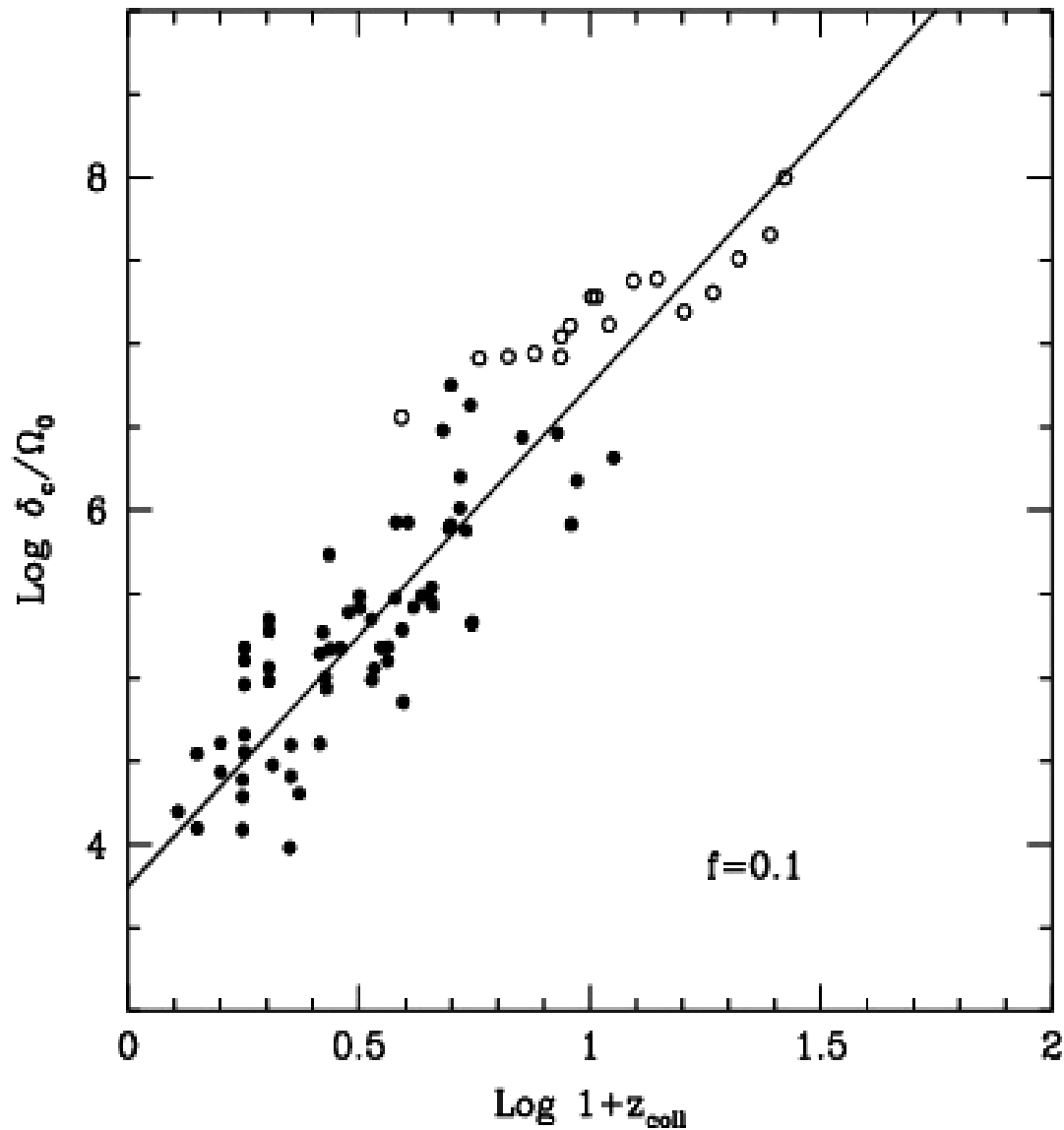
The same form fits for different cosmological parameters and power spectra of initial density perturbations.





Less massive halos
are more
concentrated

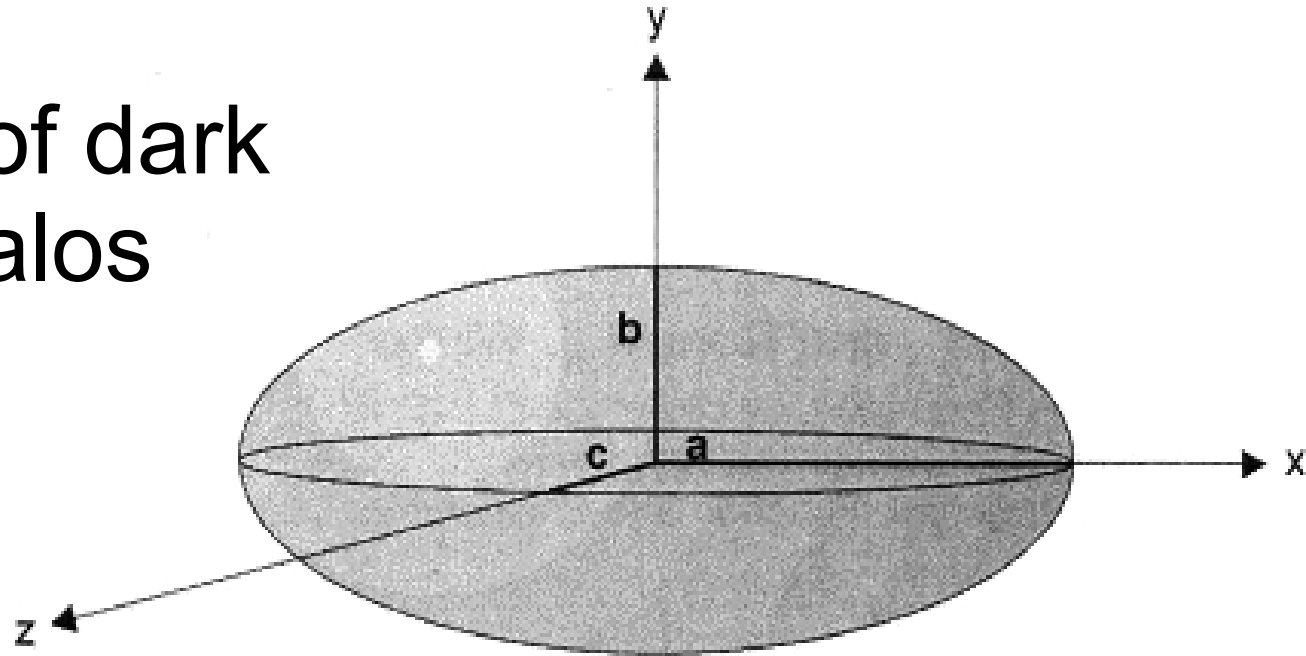




Correlation between the characteristic density of the halo and the redshift at which a given fraction of its mass “collapsed” into a virialized structure.

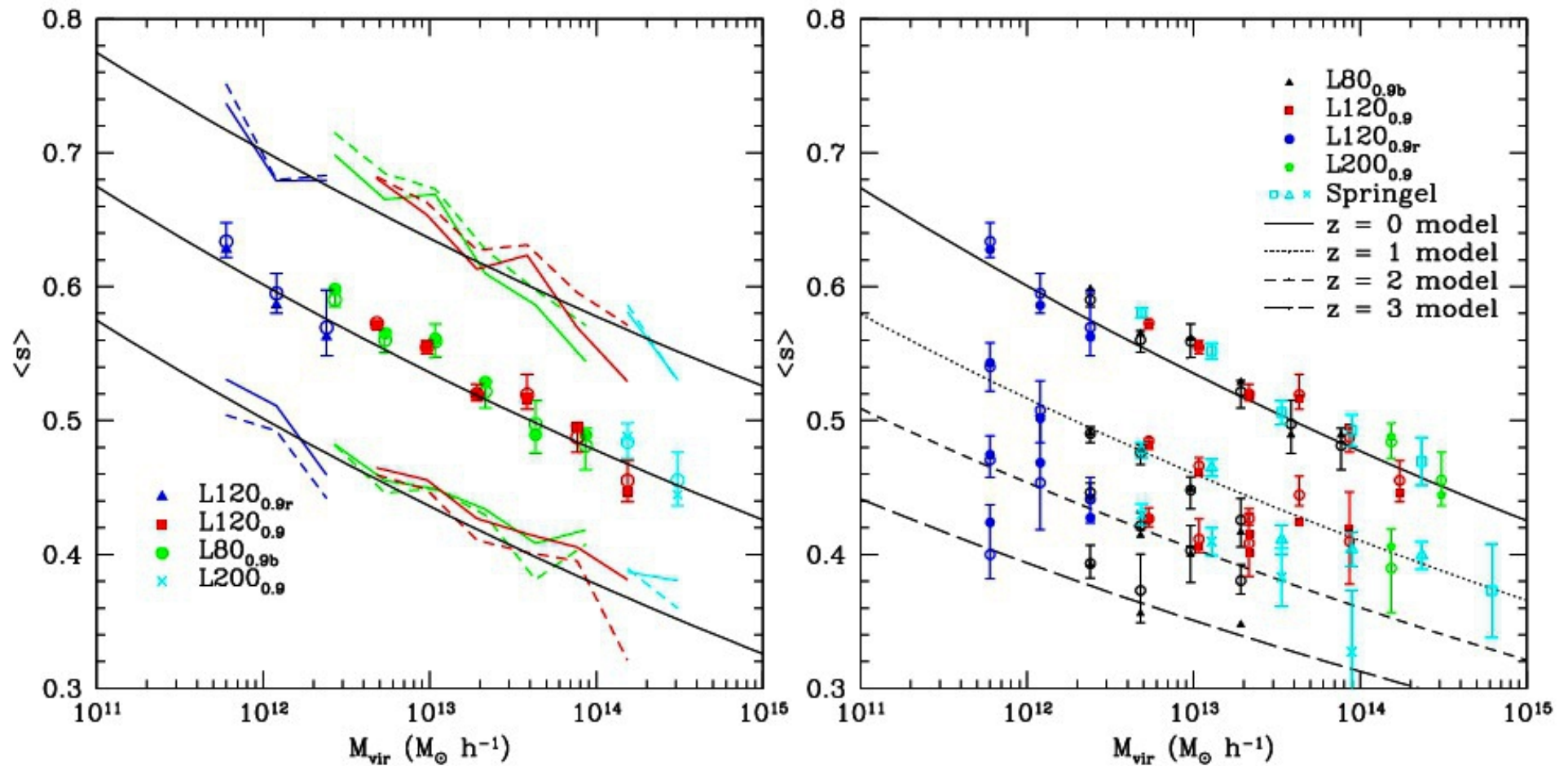
Fig. 8.— The characteristic density of all halos in our series as a function of the redshift at which half of the final mass is in collapsed progenitors more massive than 10% of the final mass. Solid

Shapes of dark matter halos



One way of quantifying the shape of a halo is to go one step beyond the spherical approximation and approximate halos by ellipsoids. Ellipsoids are characterised by three axes, a, b, c , with $a \geq b \geq c$, which are normally described in terms of ratios, $s \equiv c/a$, $q \equiv b/a$, and $p \equiv c/b$. Ellipsoids can also be described in terms of three classes, which have corresponding ratio ranges: prolate (sausage shaped) ellipsoids have $a > b \approx c$ leading to axial ratios of $s \approx q < p$, oblate (pancake shaped) ellipsoids have $a \approx b > c$ leading to axial ratios of $s \approx p < q$, and triaxial ellipsoids are in between prolate and oblate with $a > b > c$.

$s=c/a$ (ratio of the shortest-to-longest axes) decreases at high halo masses and high redshifts



Halos are rounder on the outside than on the inside

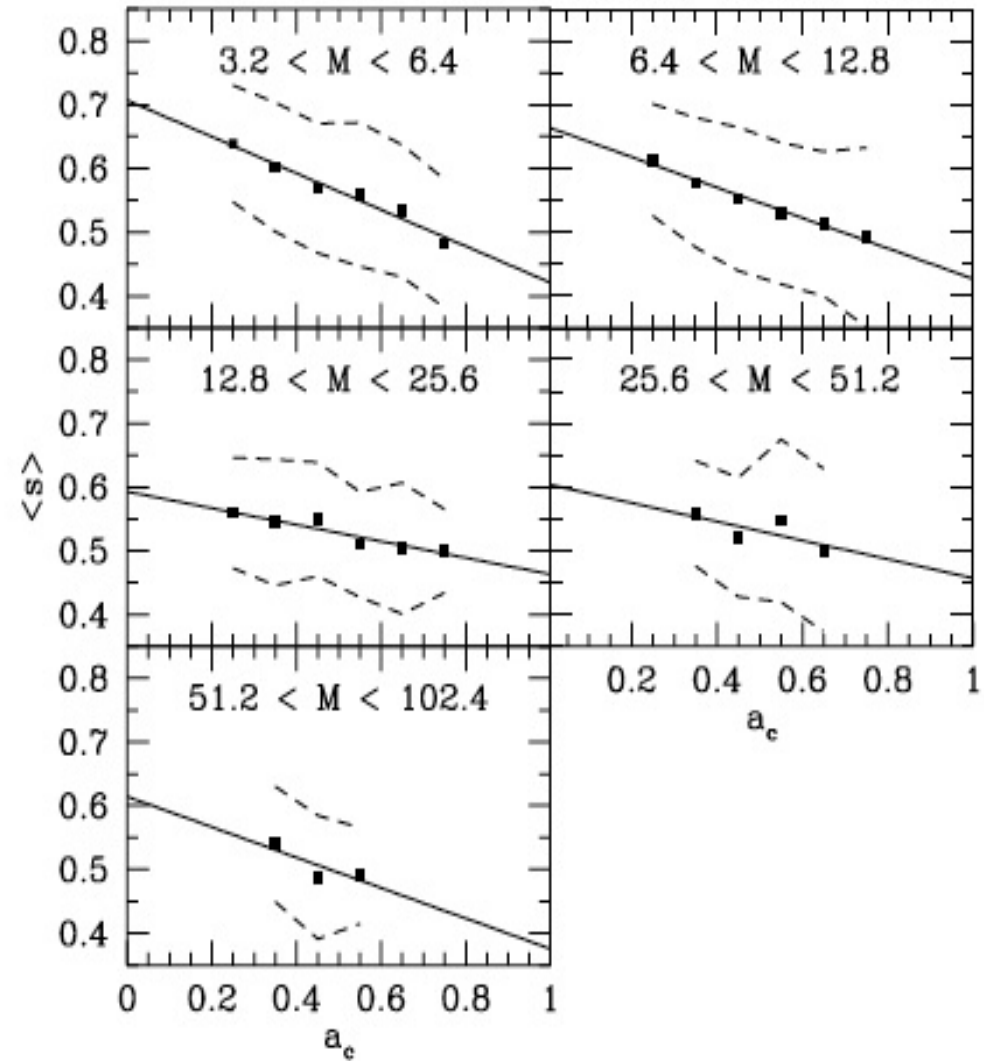
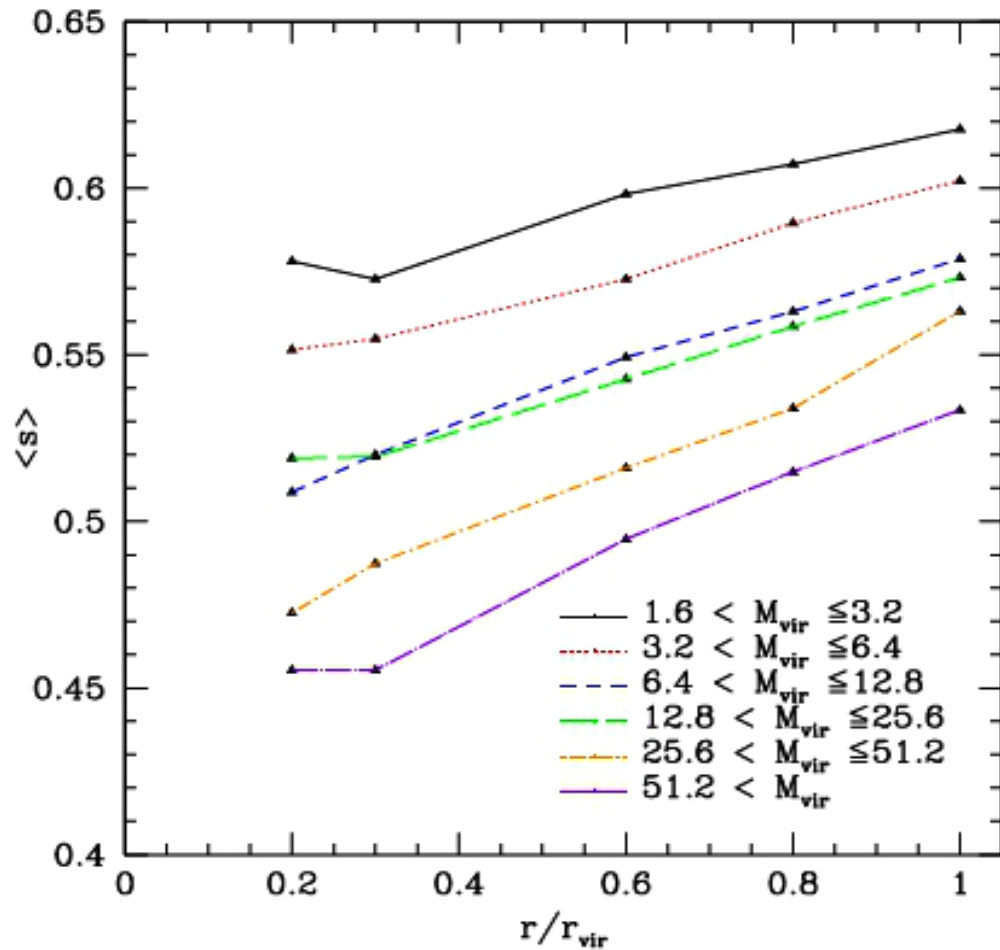
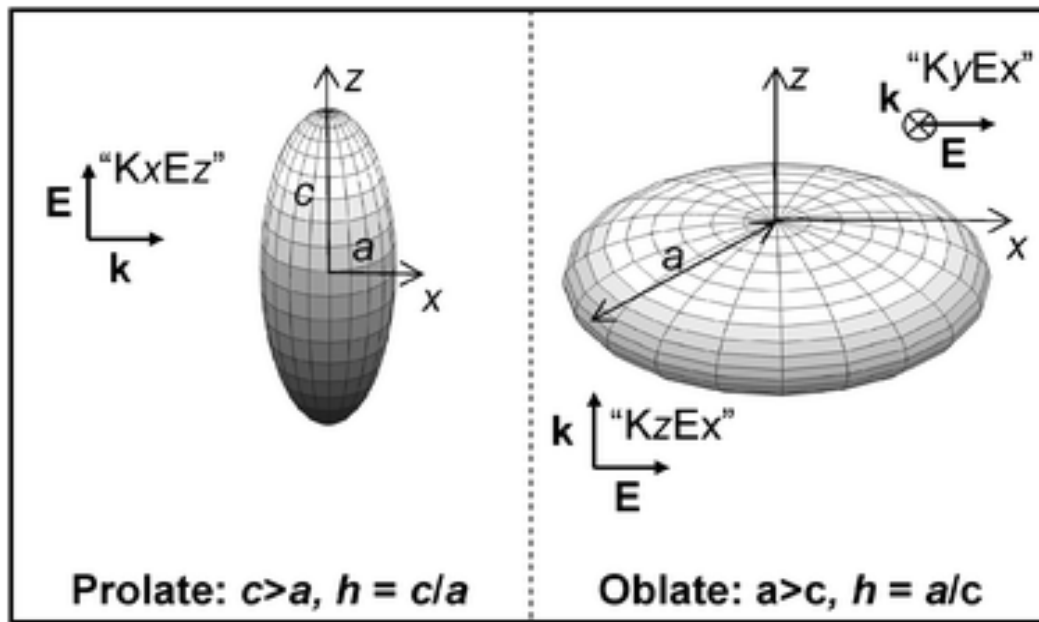


Figure 11. $\langle s \rangle$ vs characteristic formation epoch for different mass bins (mass quoted in units of $10^{12} h^{-1} M_{\odot}$). Only bins that contain at least 10 halos are shown (square points). There is a distinct trend of shape with a_c for the lower mass bins. At higher mass there is still a trend but it is uncertain how strong the trend is due to the lower number statistics. Solid black line is a linear fit to the points and dashed line is the 1σ scatter about the points.



Often ellipsoids are described in terms of their triaxiality (prolate, oblate, or triaxial). One way of expressing the triaxiality of an ellipsoid is by using the triaxiality parameter [Franx, Illingworth & de Zeeuw \(1991\)](#):

$$T \equiv \frac{a^2 - b^2}{a^2 - c^2} = \frac{1 - q^2}{1 - s^2}. \quad (12)$$

An ellipsoid is considered *oblate* if $0 < T < 1/3$, *triaxial* with $1/3 < T < 2/3$, and *prolate* if $2/3 < T < 1$. It

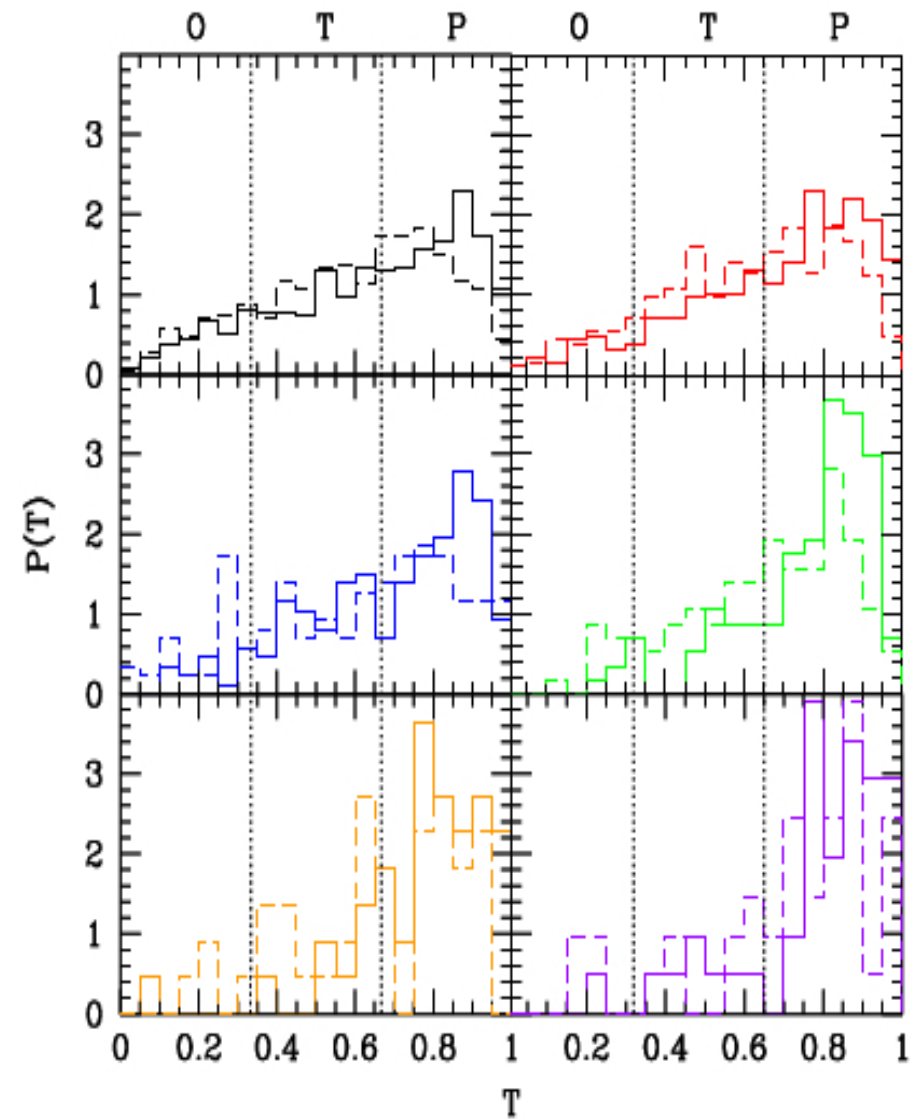


Figure 8. Triaxiality of halos at $z = 0$ at $R = 0.3R_{\text{vir}}$ (solid) and R_{vir} (dashed). Beginning with the top left histogram and moving right, then down, the triaxiality of halos is divided into the same mass bins as in Figure 7.

ANGULAR MOMENTUM OF HALOS AS CHARACTERIZED BY SPIN

The spin parameter of a halo is a dimensionless quantity introduced by Peebles (1969) that indicates the amount of ordered rotation compared to the internal random motions. For a halo of mass M and angular momentum J it is defined as

$$\lambda = \frac{|J| |E|^{1/2}}{GM^{5/2}}, \quad (3)$$

where the total energy $E = T + U$ with T the kinetic energy of the halo after subtracting its bulk motion and U the potential energy of the halo produced by its own mass distribution.

The specific angular momentum j and kinetic energy T of each halo containing N_p particles are given by:

$$j = \frac{1}{N_p} \sum_{i=1}^{N_p} \mathbf{r}_i \times \mathbf{v}_i$$

$$T = \frac{1}{2} M_h \sum_{i=1}^{N_p} v_i^2$$

where \mathbf{r}_i is the position vector of particle i relative to the halo centre, and \mathbf{v}_i is its velocity relative to the halo centre of momentum.

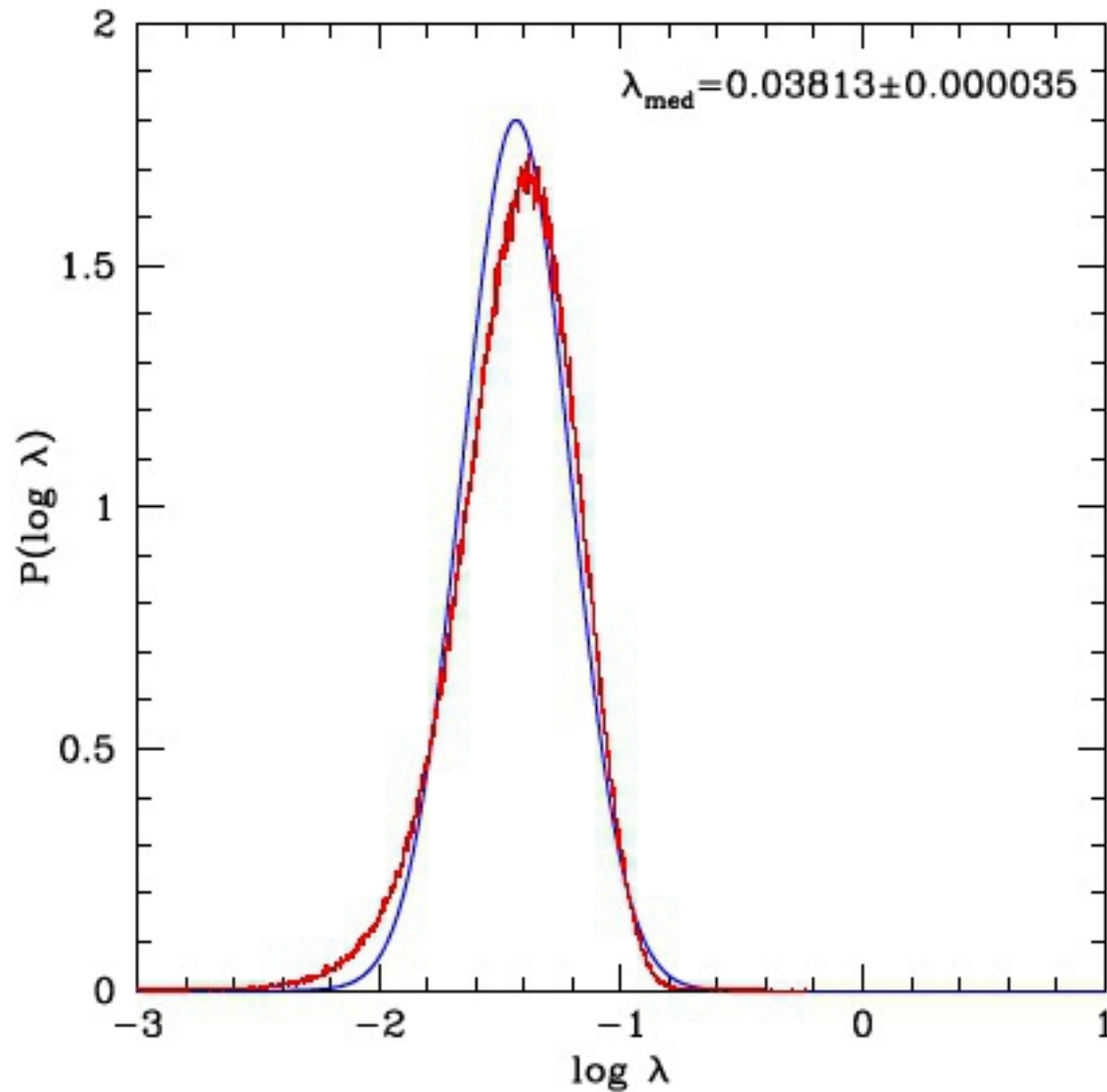
The halo potential energy, U , is calculated using all halo particles if $M_h \leq 1000m_p$, and is rescaled up from that of 1000 randomly-sampled particles otherwise. The potential is that used in the simulation itself:

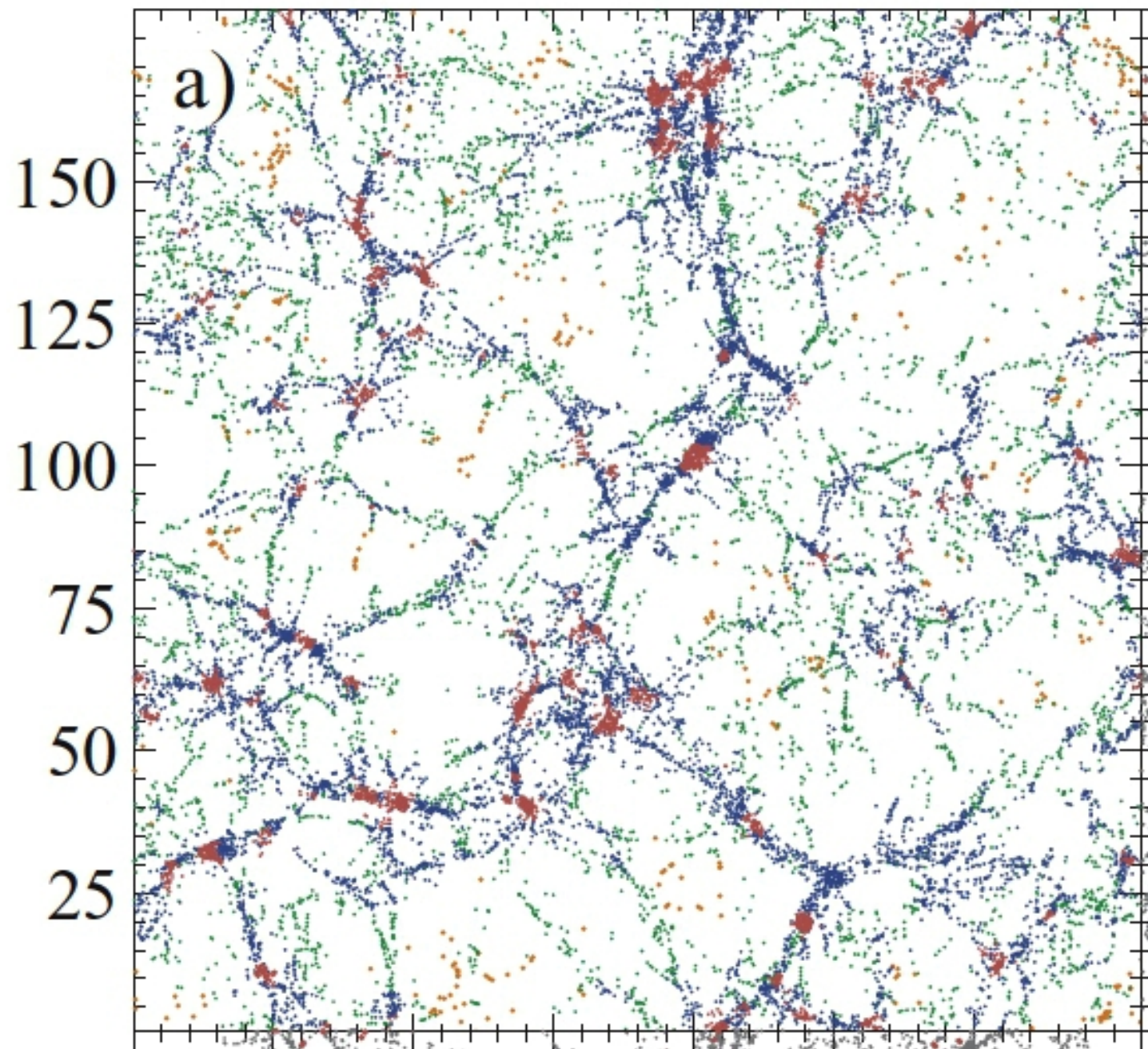
$$U = \left(\frac{N_p^2 - N_p}{N_{\text{sel}}^2 - N_{\text{sel}}} \right) \left(\frac{-Gm_p^2}{\eta} \right) \sum_{i=1}^{N_{\text{sel}}-1} \sum_{j=i+1}^{N_{\text{sel}}} -W_2(r_{ij}/\eta)$$

where N_{sel} is the number of selected particles ($N_{\text{sel}} \leq 1000$), η is the softening length (see Table 1), r_{ij} is the magnitude of the separation vector between the i th and j th particles in the halo, and the softening kernel (see Springel et al. 2001) is:

$$W_2(u) = \begin{cases} \frac{16}{3}u^2 - \frac{48}{5}u^4 + \frac{32}{5}u^5 - \frac{14}{5}, & 0 \leq u \leq \frac{1}{2}, \\ \frac{1}{15u} + \frac{32}{3}u^2 - 16u^3 + \frac{48}{5}u^4 \\ \quad - \frac{32}{15}u^5 - \frac{16}{5}, & \frac{1}{2} \leq u \leq 1, \\ -\frac{1}{u}, & u \geq 1 \end{cases}$$

$$P(\log \lambda) = \frac{1}{\sigma_{\lg} \sqrt{2\pi}} \exp \left[-\frac{\log^2 (\lambda/\lambda_0)}{2\sigma_{\lg}^2} \right]$$





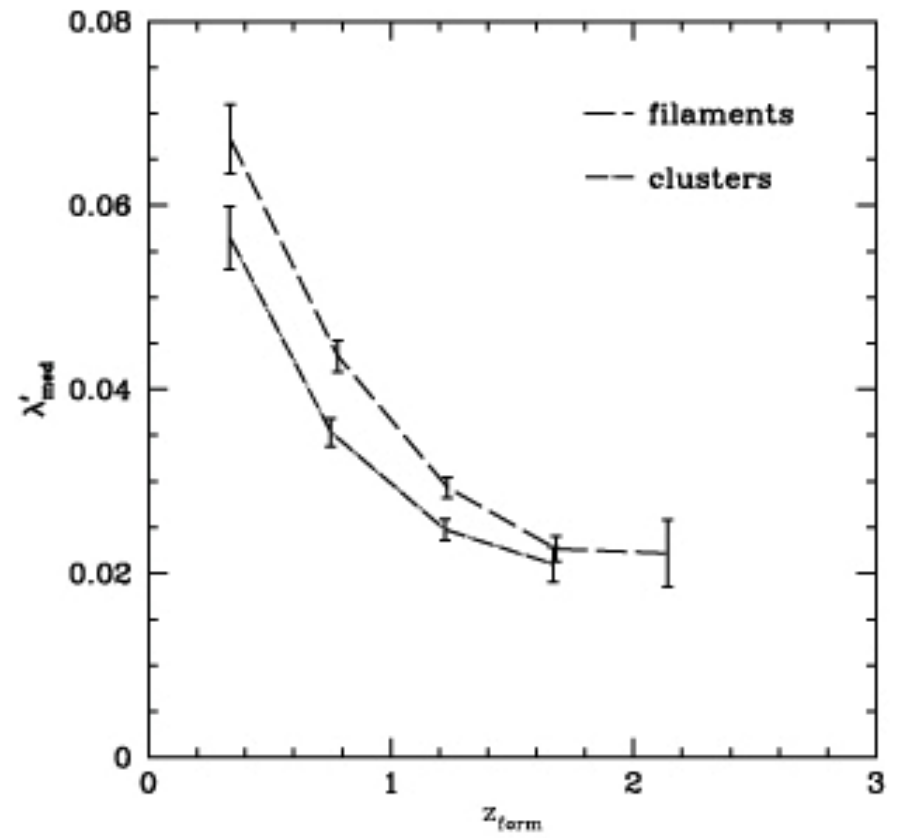
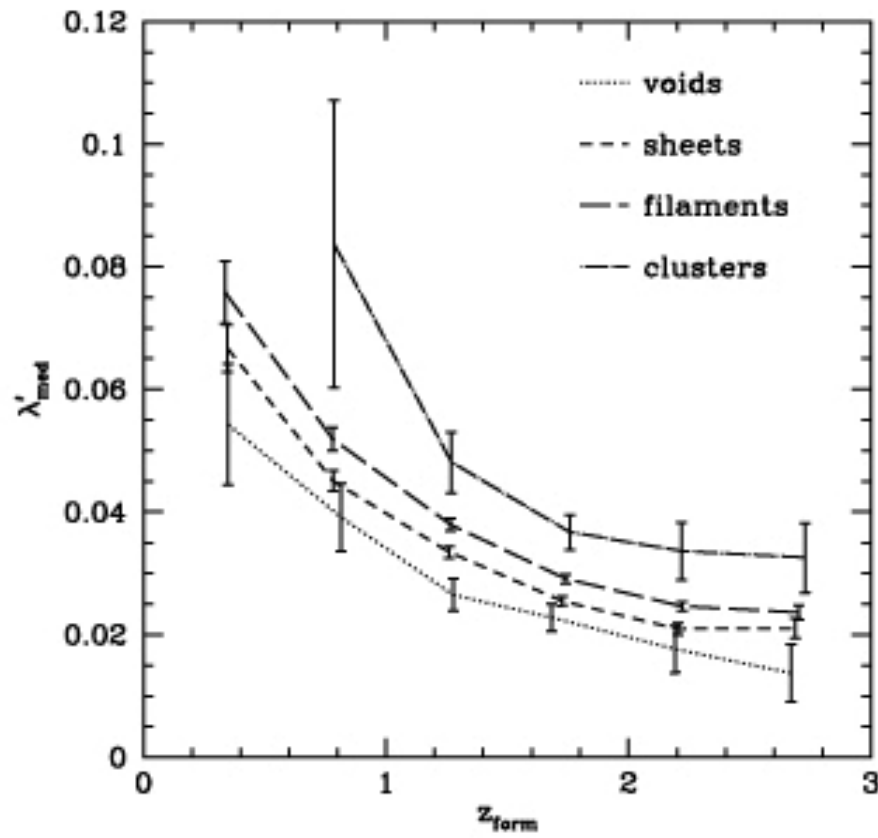
Clusters

Filaments

Sheets

Voids

Spin is higher in denser environments



Sphericity and Triaxiality only Weakly Dependent on Environment

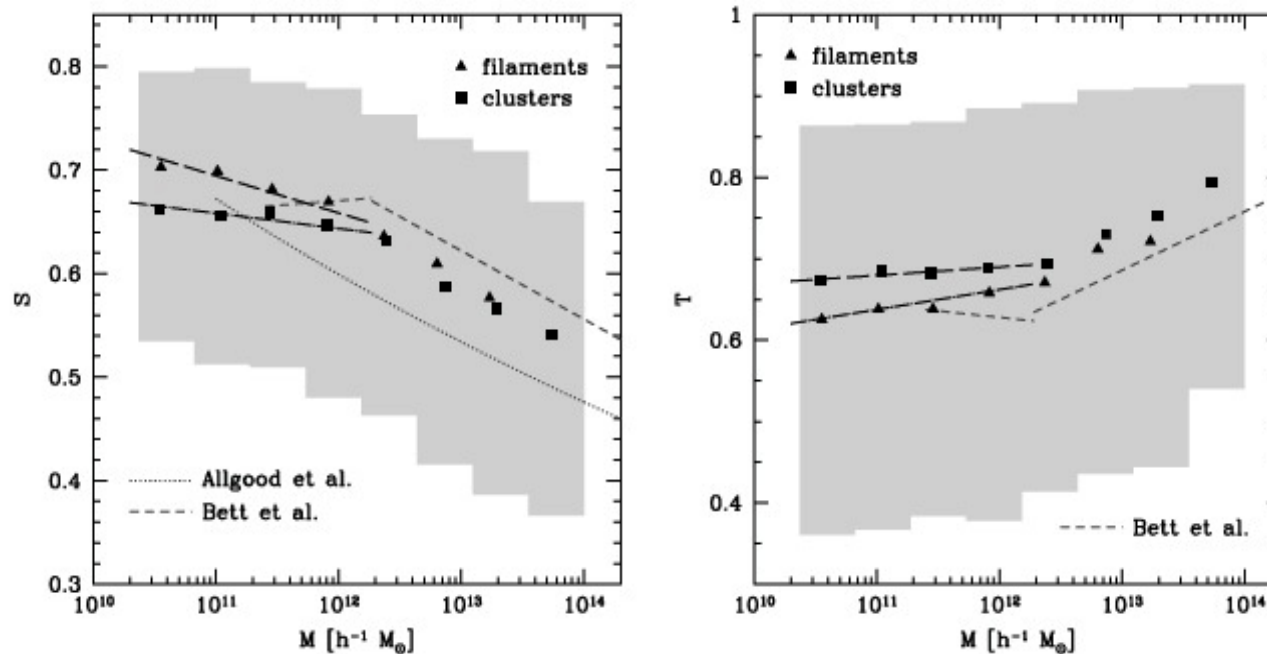
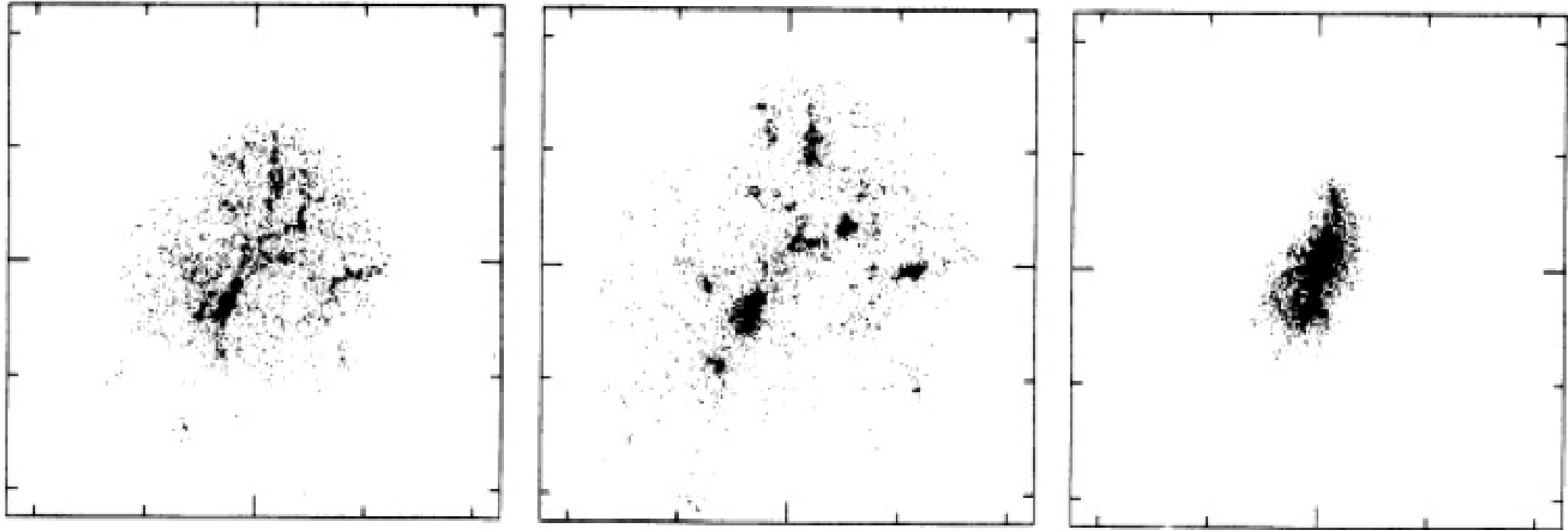


Figure 5. Median halo sphericity (left-hand panel) and triaxiality (right-hand panel) as a function of halo mass for haloes in filaments and clusters. The behaviour for haloes in sheets is almost identical to that for filaments. The shaded area indicates the central 1σ scatter in the whole sample, not split by environment. The dark grey lines indicate the fits of Allgood et al. (2006) for S and Bett et al. (2006) for S and T , the black lines show our fits to haloes with masses $M < 2 \times 10^{12} h^{-1} M_{\odot}$. Parameters are given in Section 4.2.

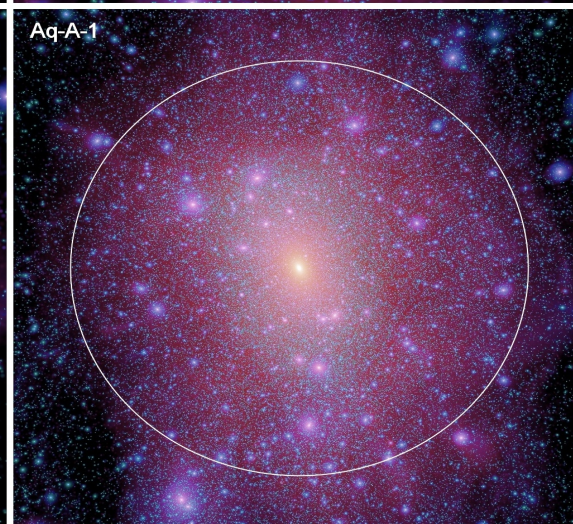
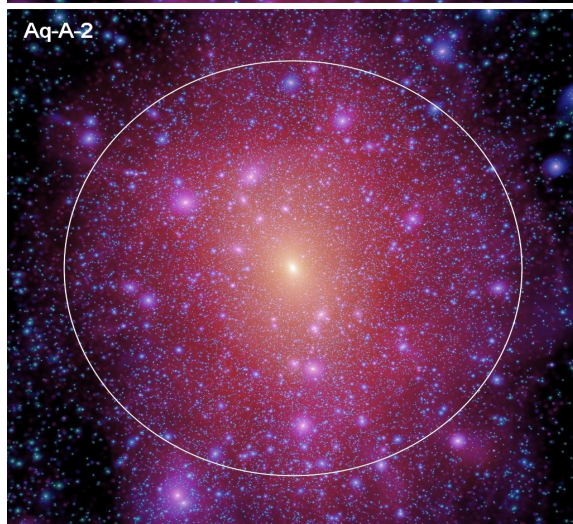
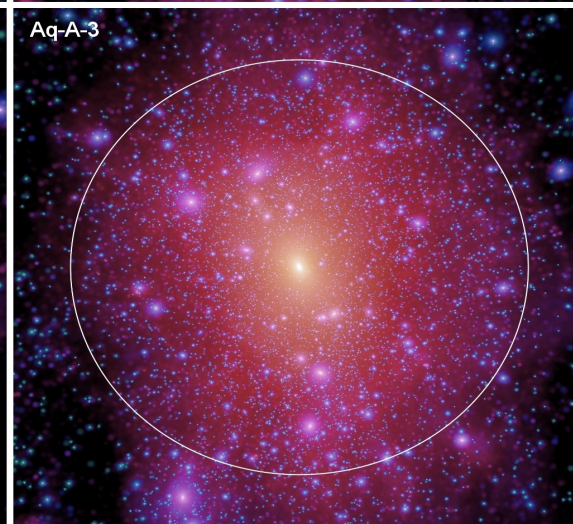
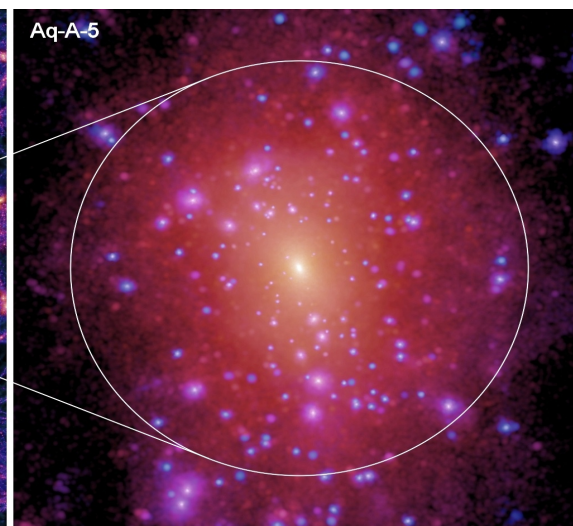
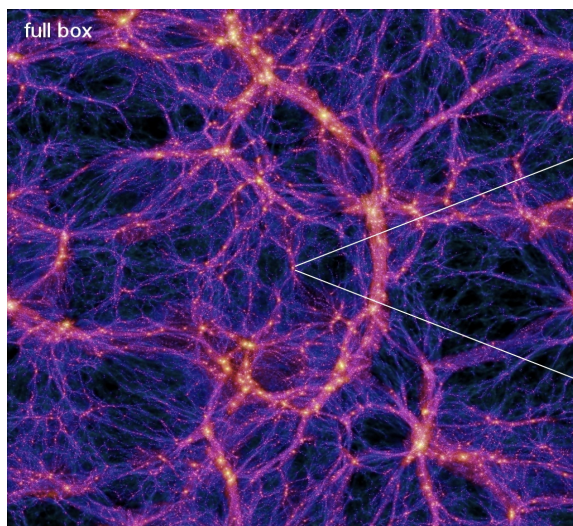
Substructure in Dark Matter Halos

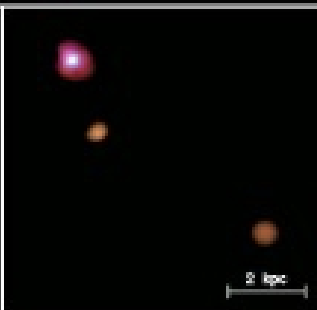
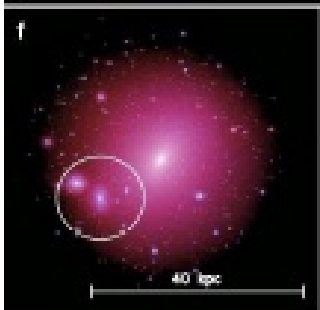
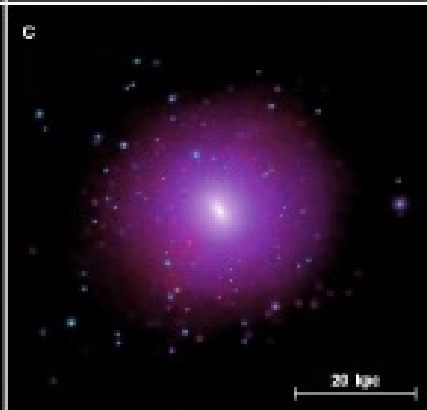
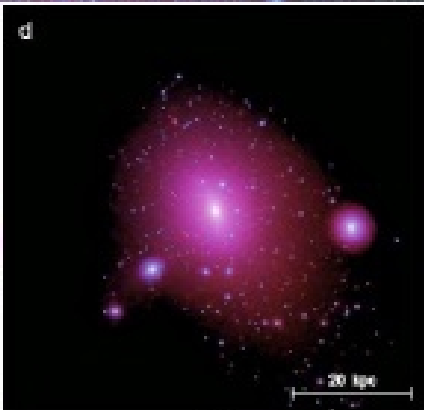
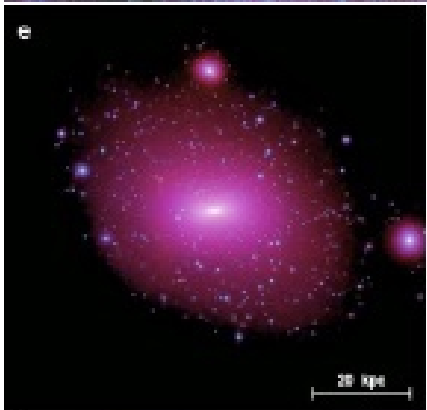
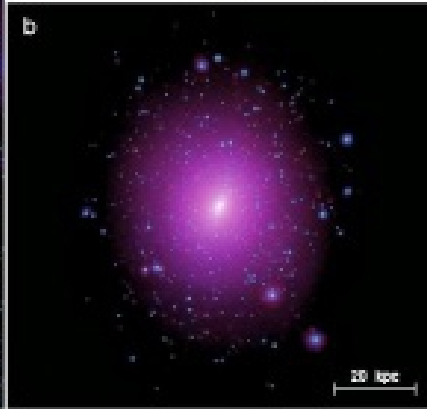
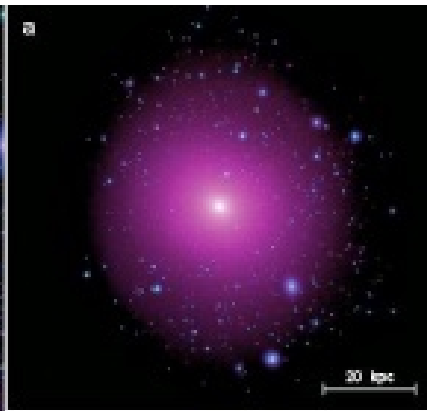
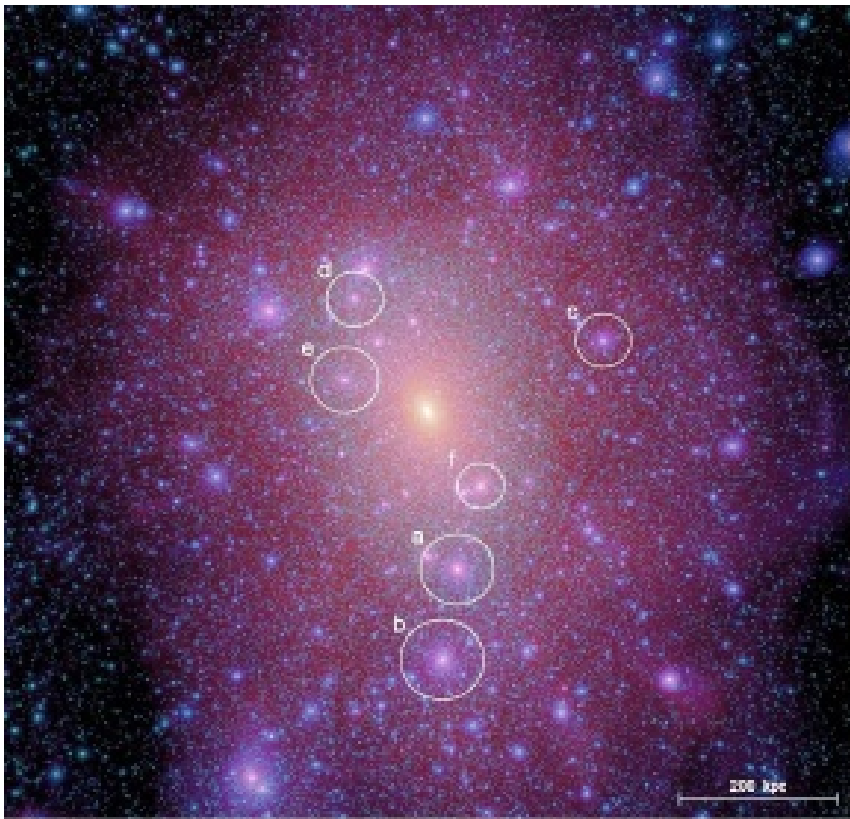


Early halos in simulations exhibited very little substructure – this was known as the “overmerging problem”, because bound, virialized systems of multiple galaxies do exist (galaxy groups and clusters).

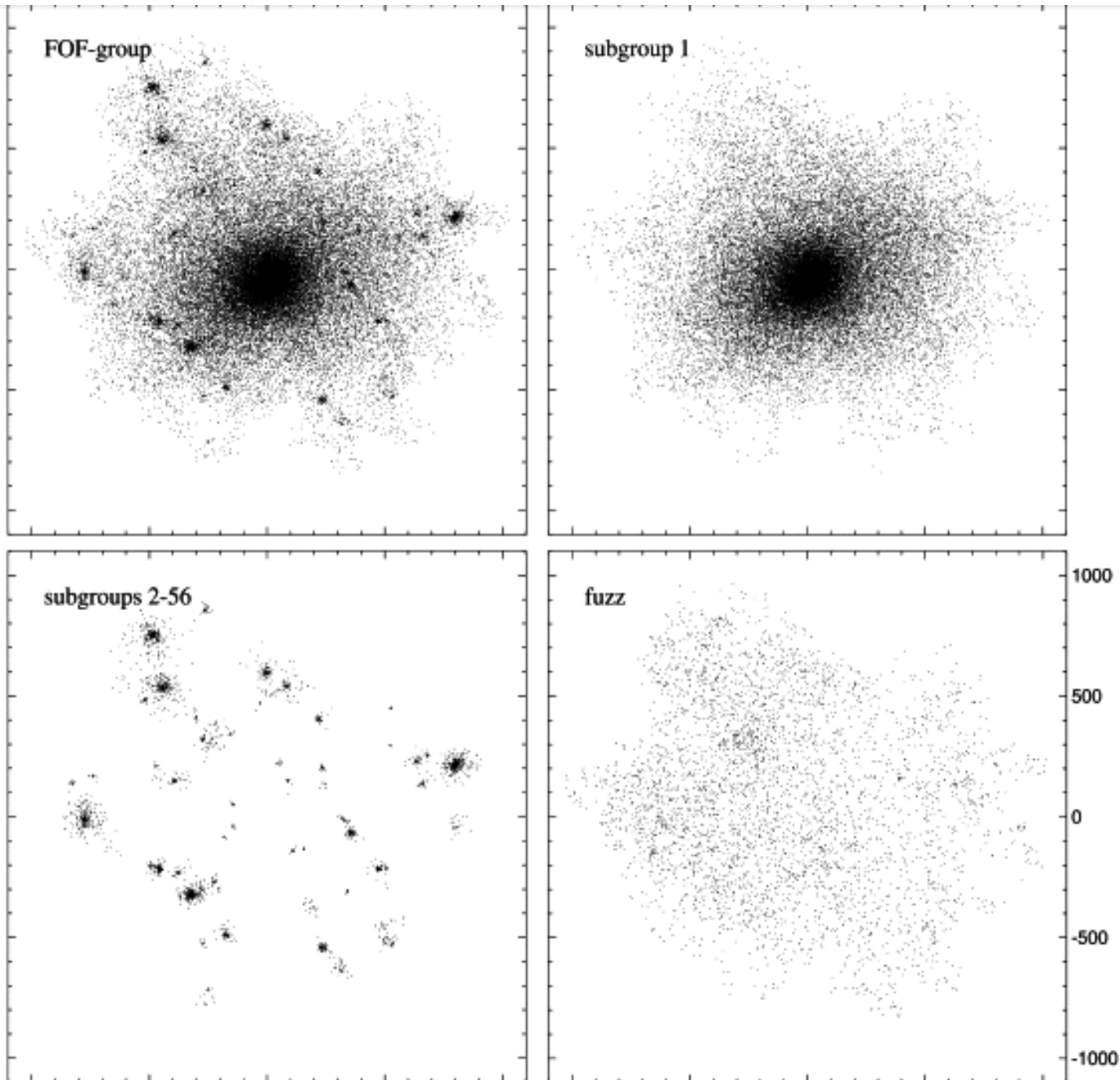
As computers became more powerful, simulations of every increasing particle number could be carried out. The higher resolution simulations revealed a rich hierarchy of substructure in dark matter halos.

Aquarius simulations contains six examples of an isolated halo similar in mass to that of the Milky Way. These are simulated in their full cosmological context (assuming the concordance Λ CDM cosmology) and at various resolutions up to about 200 million particles (counted within the radius where the enclosed density is 200 times the cosmic mean). One halo is also simulated at even higher resolution, resulting in almost 1.5 billion particles within this radius.



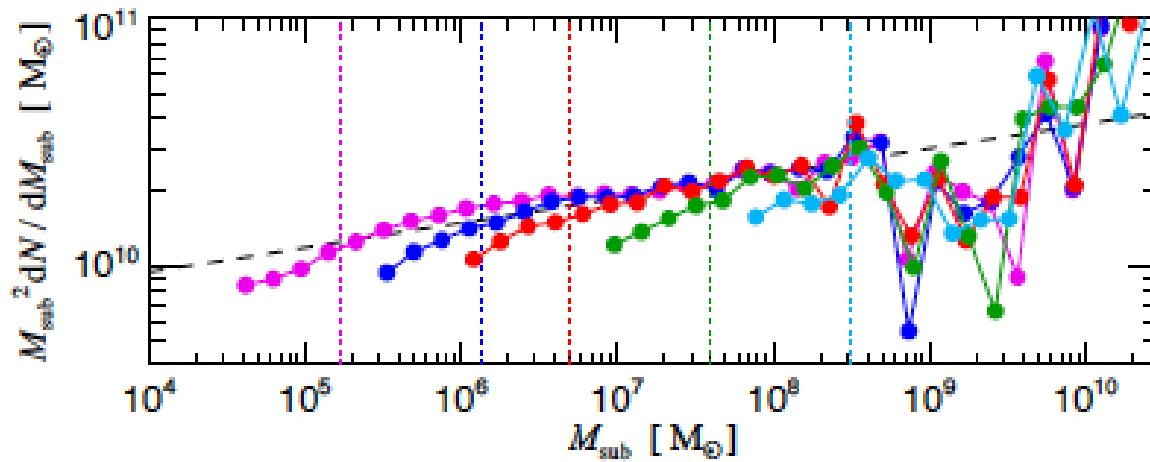
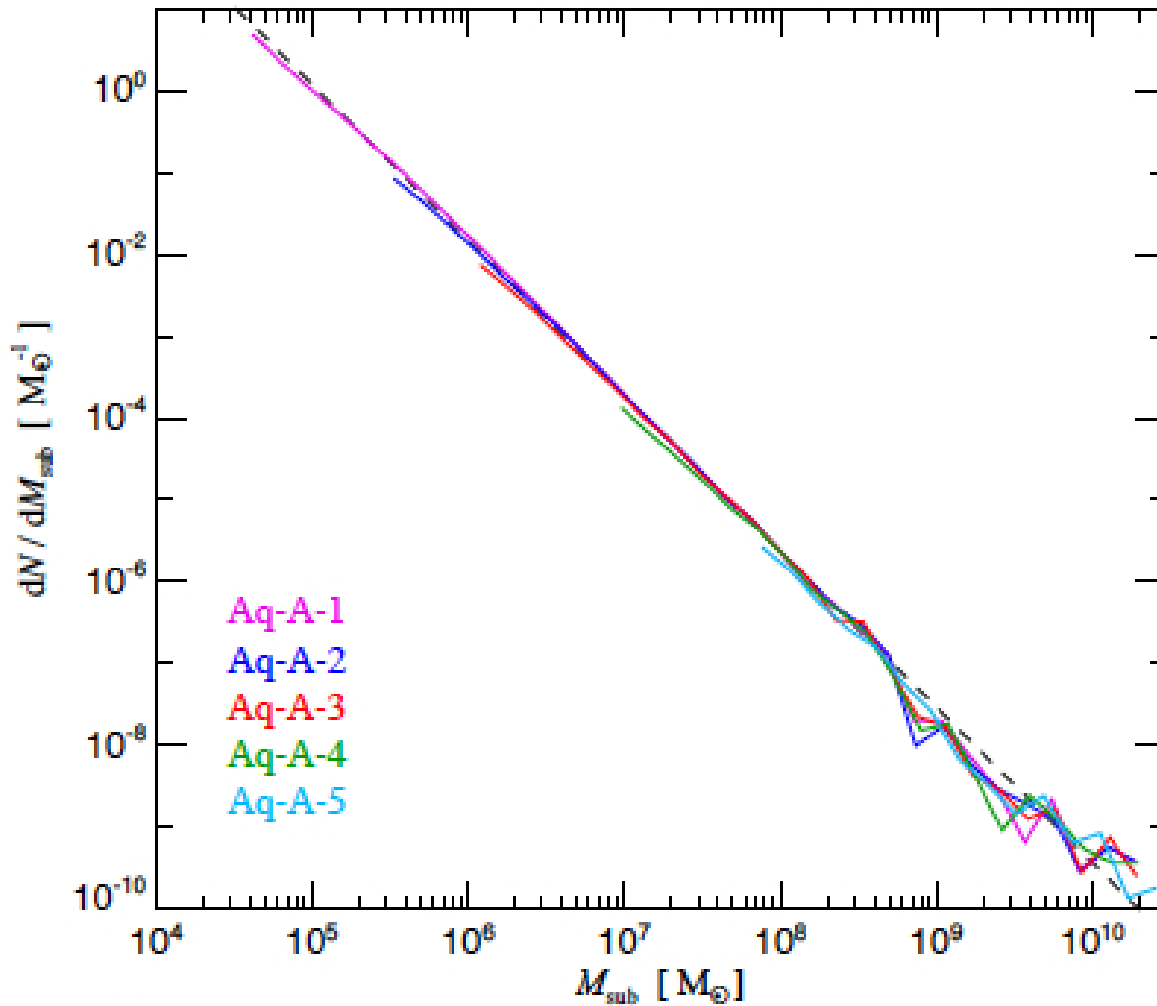


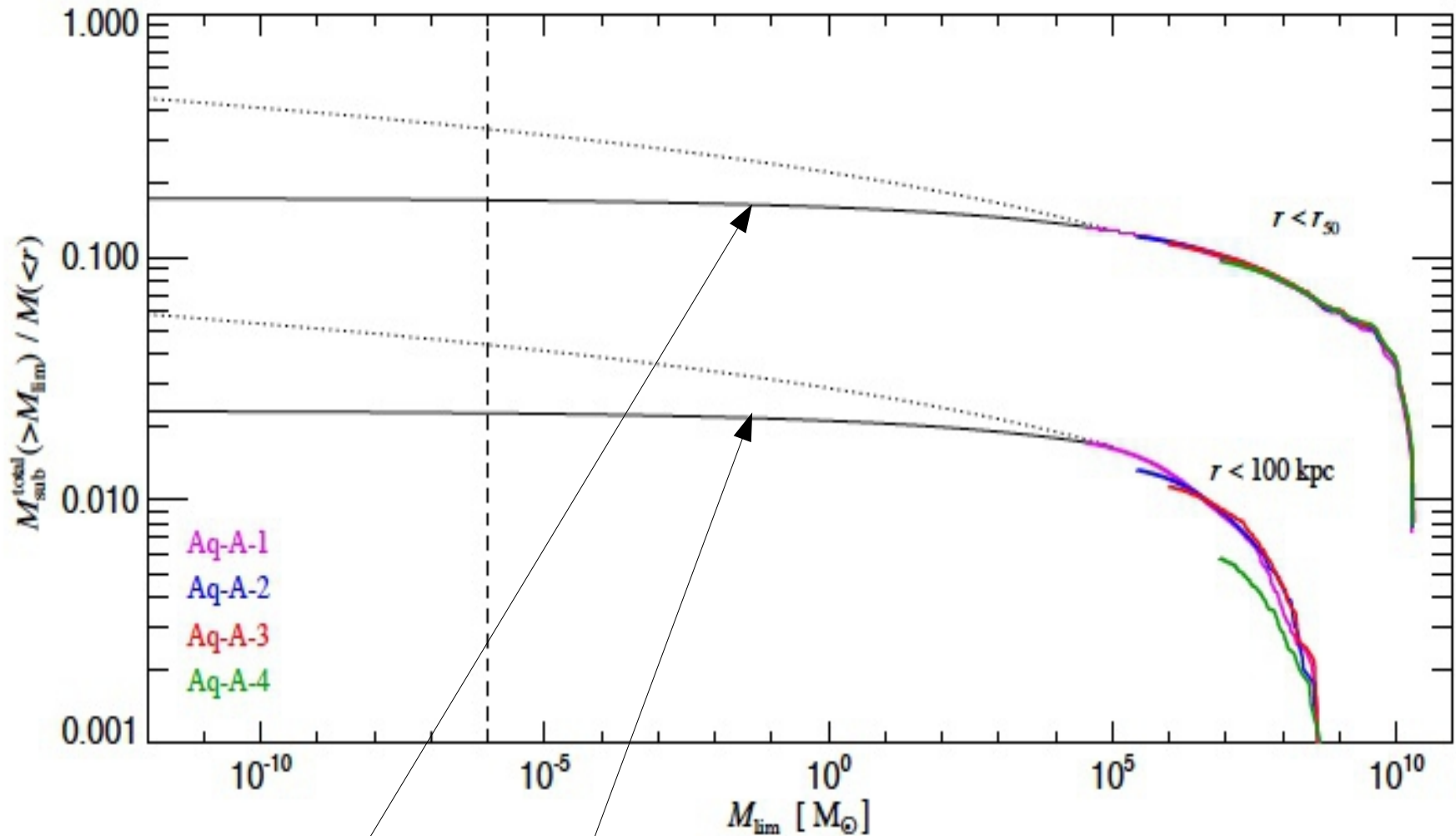
In the highest resolution simulation, one even finds “substructures within substructures”



Sub-halo identification algorithms, eg. SUBFIND (Springel et al 2001) employ a variable link-length/density threshold to identify local density maxima on top of the global one.

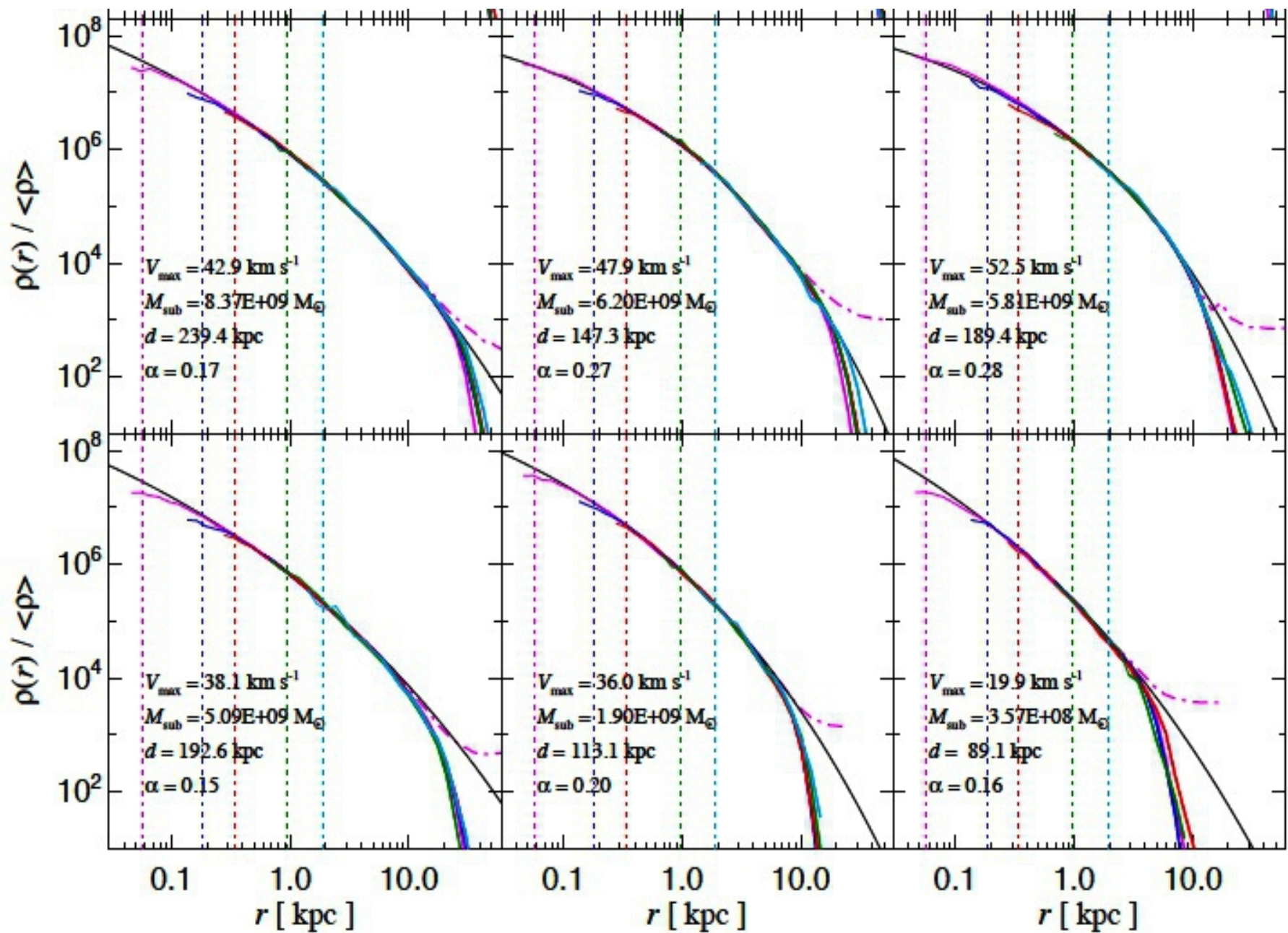
Subhalo mass function is a power law with slope -1.9

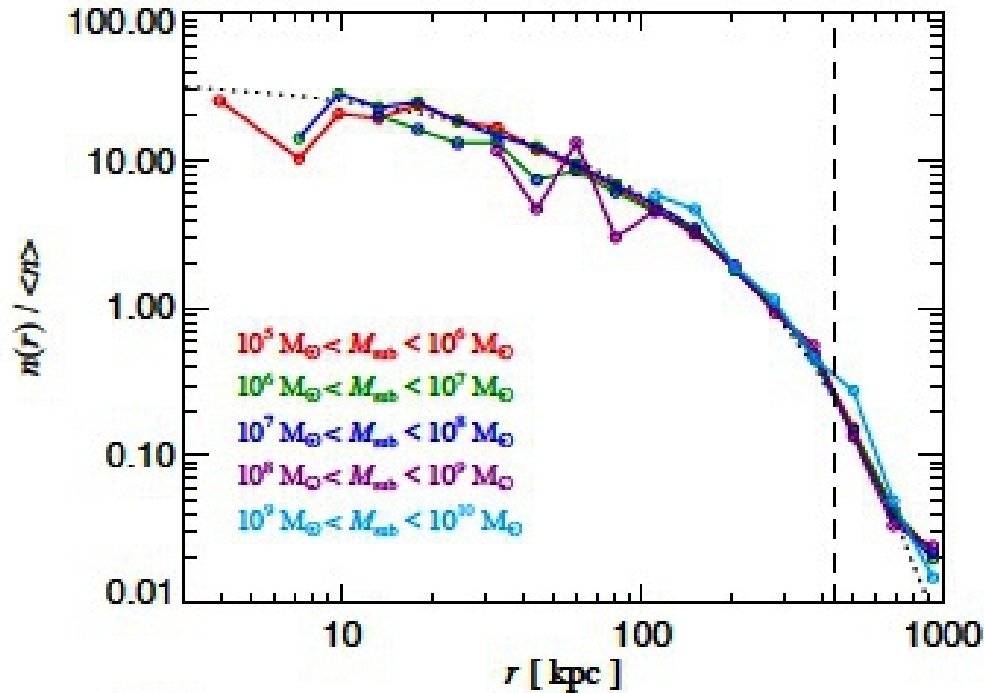




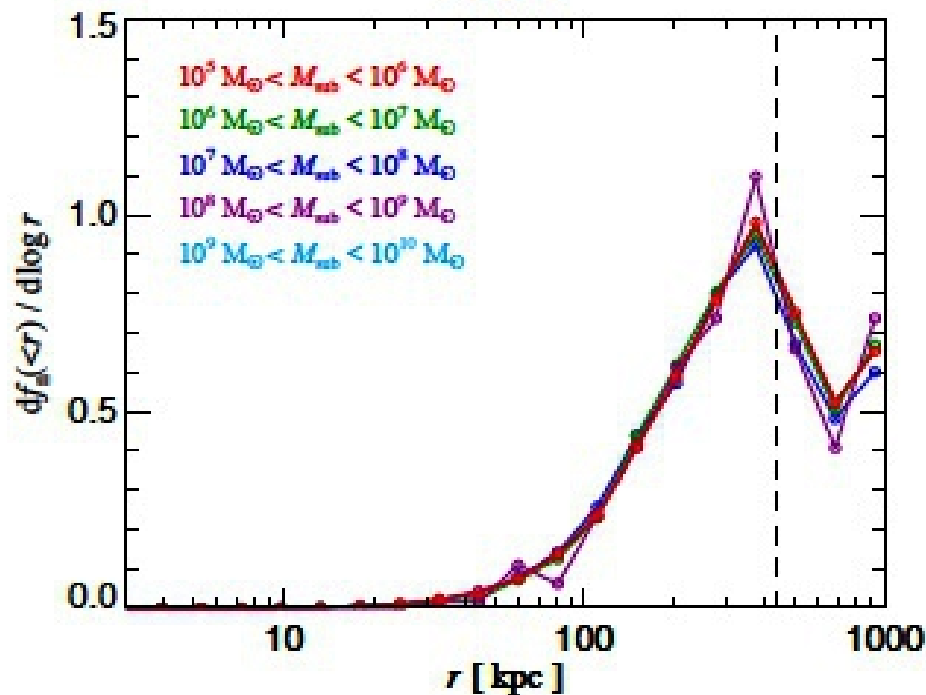
Substructure mass function extrapolated using -1.9 power law: less than 0.2 with the half-mass radius

Density profiles of subhalos





Subhalo density profile is independent of subhalo mass.



Number fraction of subhalos per logarithmic interval in radius. The area under the curves is proportional to subhalo number, showing that most subhalos are found in the outermost parts of the halo.

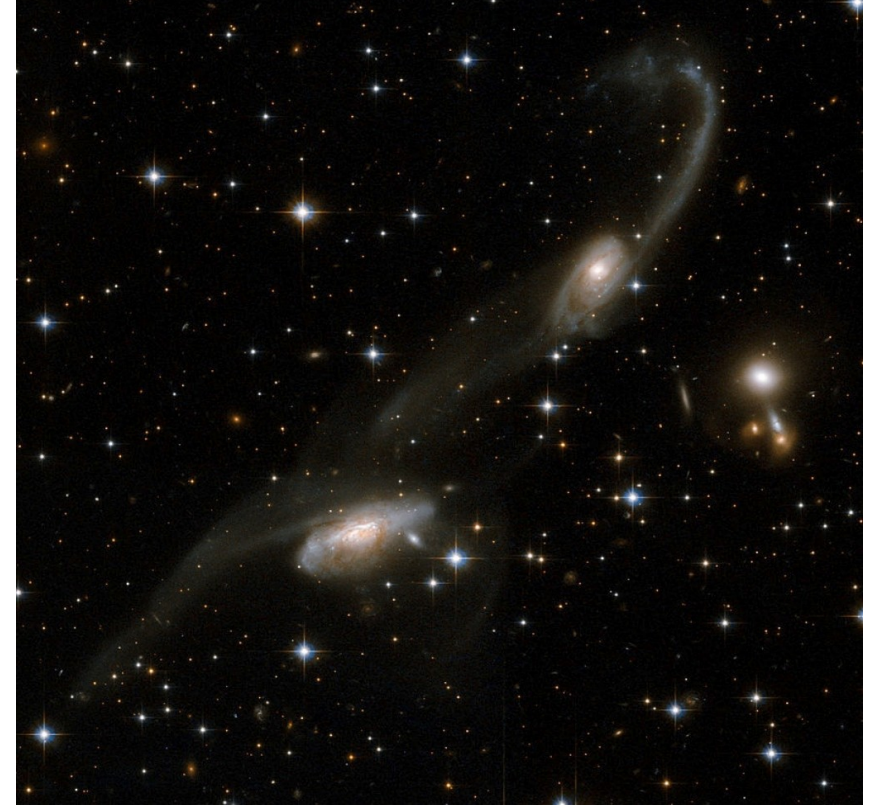
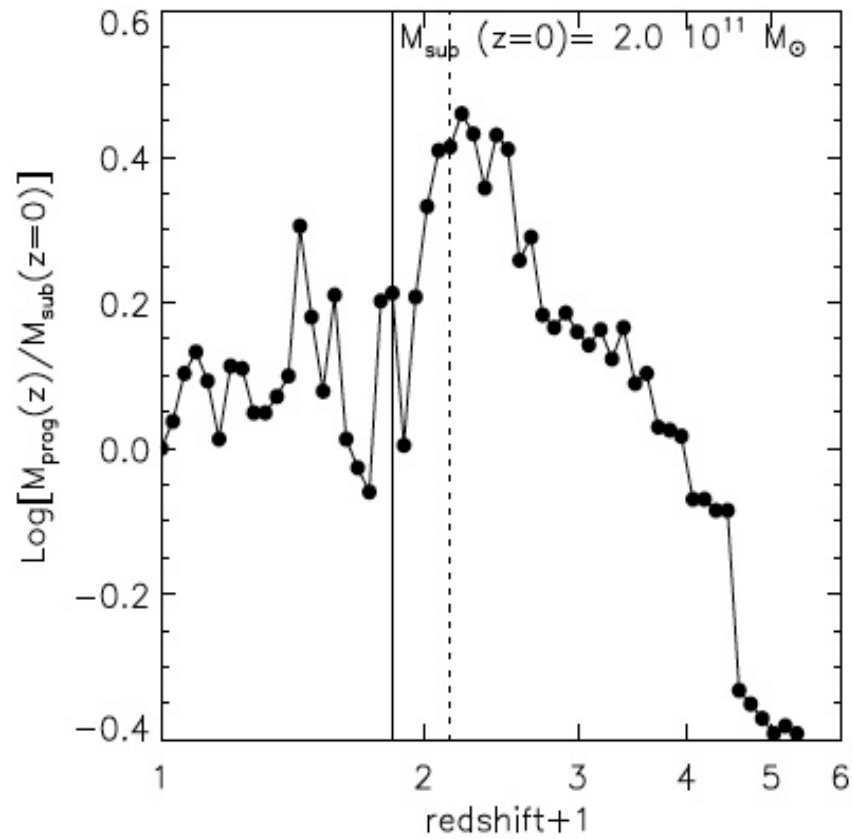
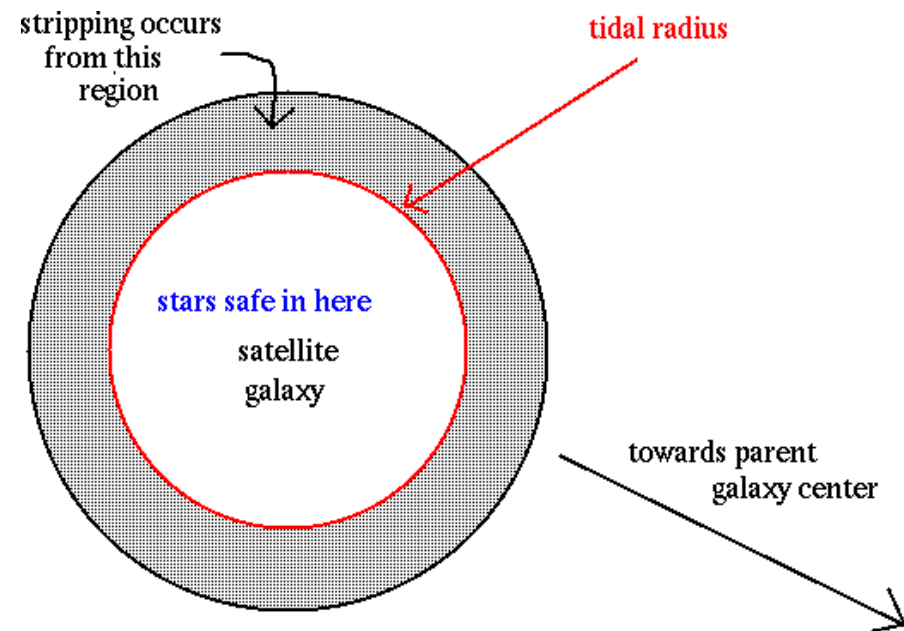
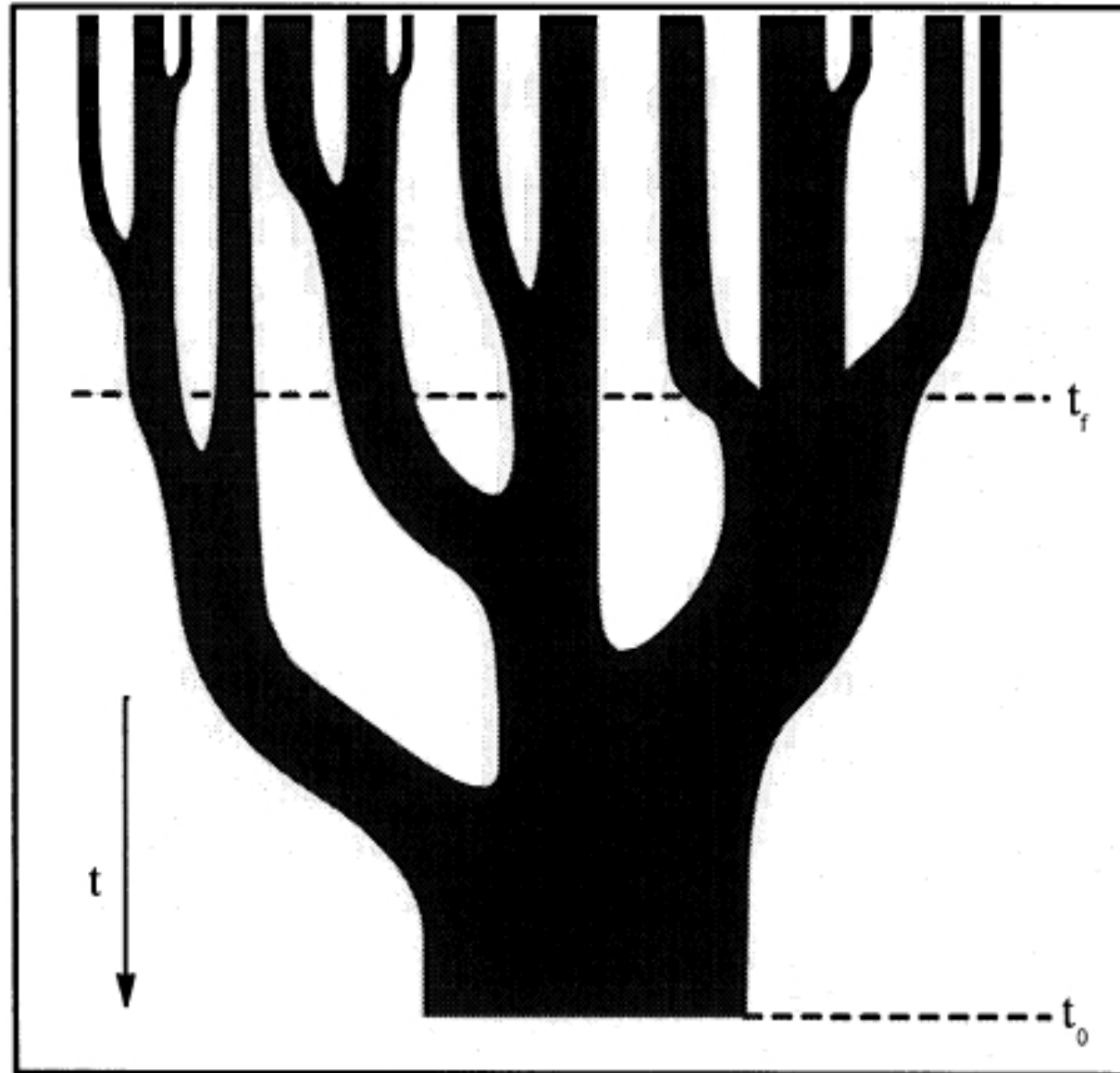


Figure 9. Example for a typical mass accretion history for a subhalo of mass $2 \times 10^{11} h^{-1} M_{\odot}$ (lower panel), and the corresponding variation of mass for the parent halo in which the subhalo resides (top panel). The vertical solid line corresponds to the last time the subhalo is outside the main progenitor of the cluster; the dotted line corresponds to the time the subhalo becomes a substructure



Merger histories of dark matter halos



Lacey & Cole 1993: Derive approximate merger histories analytically by starting with the linear density field of fluctuations and allowing the smoothing scale is changed.

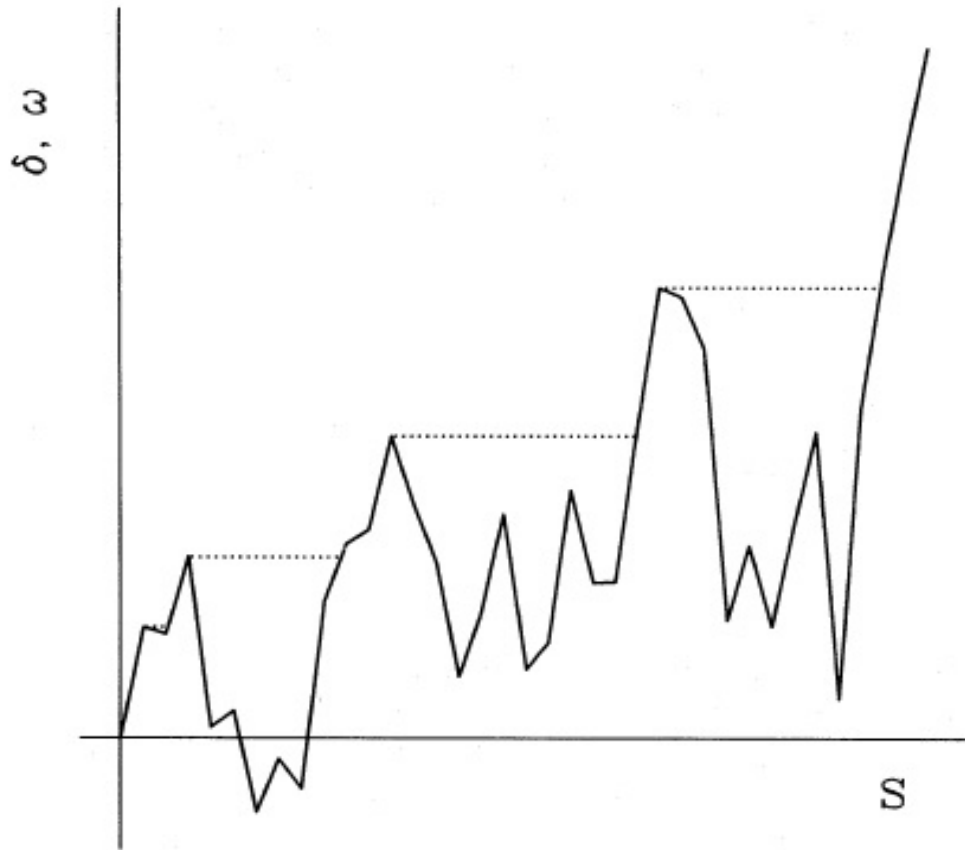


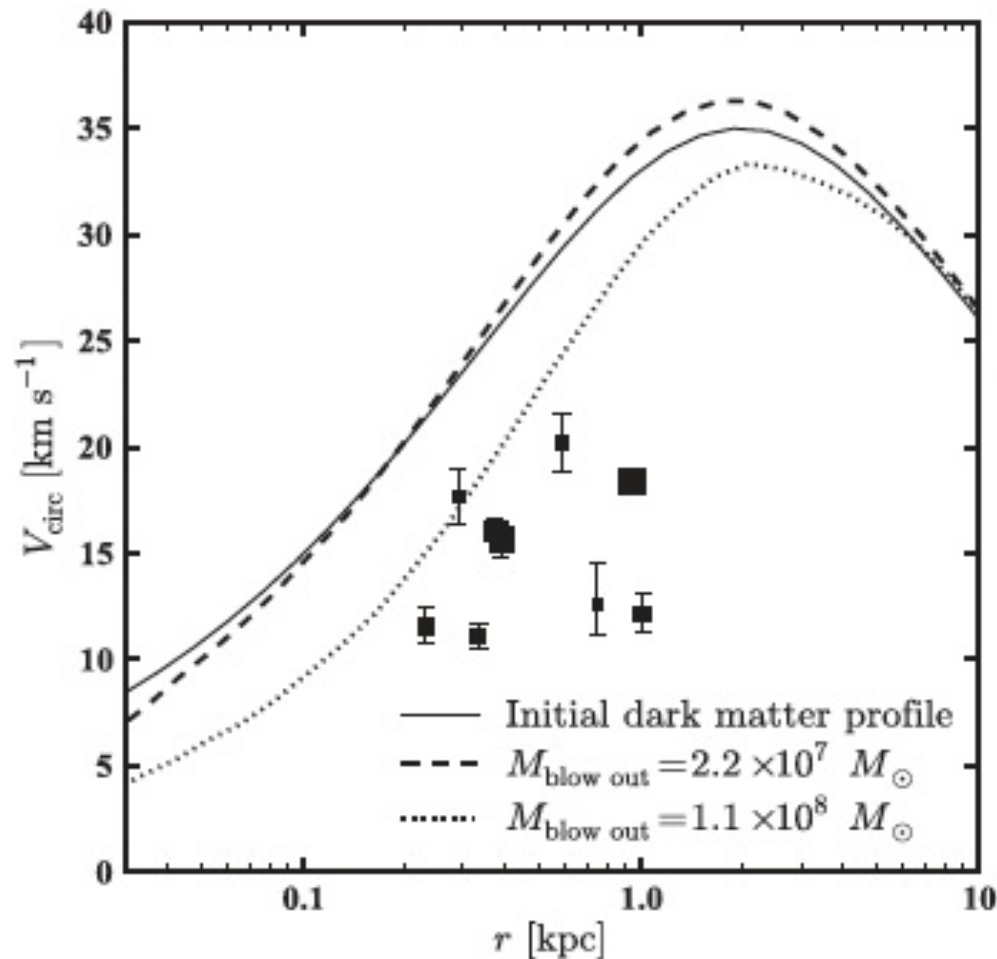
Figure 1. A trajectory $\delta(S)$, and the corresponding halo merger history. The solid line shows the trajectory for the overdensity δ as the smoothing scale is varied. The dotted line shows the trajectory for the halo mass, represented by a function $S(\omega)$. Where δ is increasing with S , the dotted line coincides with the solid line.

We wish to determine the merger probability per unit time for a halo of given mass M at time t . Let us therefore consider the subset of trajectories, depicted in Fig. 2, which make their first upcrossing of a barrier of height ω_2 at S_2 and then continue until they eventually cross a second barrier of height $\omega_1 > \omega_2$ at various values $S_1 > S_2$. These trajectories represent haloes which at the time corresponding to ω_1 have masses corresponding to S_1 , and which by the later time corresponding to ω_2 have merged to form a halo of mass corresponding to S_2 . The conditional probability

$$f_{S_1}(S_1, \omega_1 | S_2, \omega_2) dS_1$$

$$= \frac{(\omega_1 - \omega_2)}{(2\pi)^{1/2} (S_1 - S_2)^{3/2}} \exp\left[-\frac{(\omega_1 - \omega_2)^2}{2(S_1 - S_2)}\right] dS_1$$

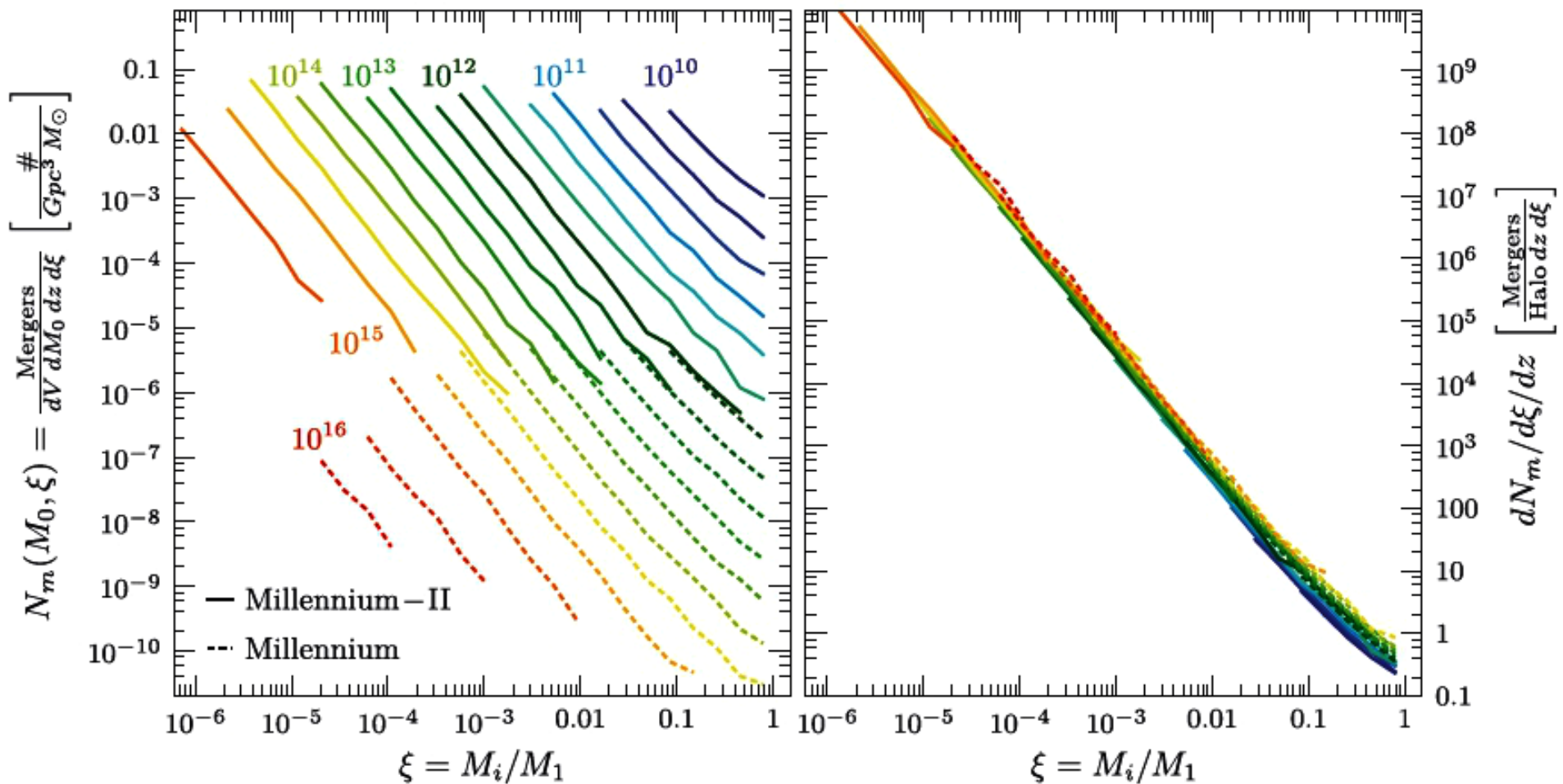
$$(S_1 > S_2, \omega_1 > \omega_2),$$



But can this work in practice?

Figure 8. Simulations of impulsive blow-out from a $V_{\max} = 35 \text{ km s}^{-1}$ halo. The initial halo profile is plotted as a solid line; the dashed and dotted curves correspond to the final, relaxed profile after gas blow-out of 2.2×10^7 and $1.1 \times 10^8 M_{\odot}$, respectively. Measured values of V_{circ} for the bright dSphs are plotted as the squares, sized proportional to $\log L_V$, with error bars. We emphasize that the two data points closest to the halo line post-blowout are among the least luminous dwarfs we consider [Draco and Ursa Minor, with $L_V \simeq (2-4) \times 10^5$]. Matching their densities via impulsive feedback would then require ejecting ~ 100 times as much mass as is present in stars today in these systems.

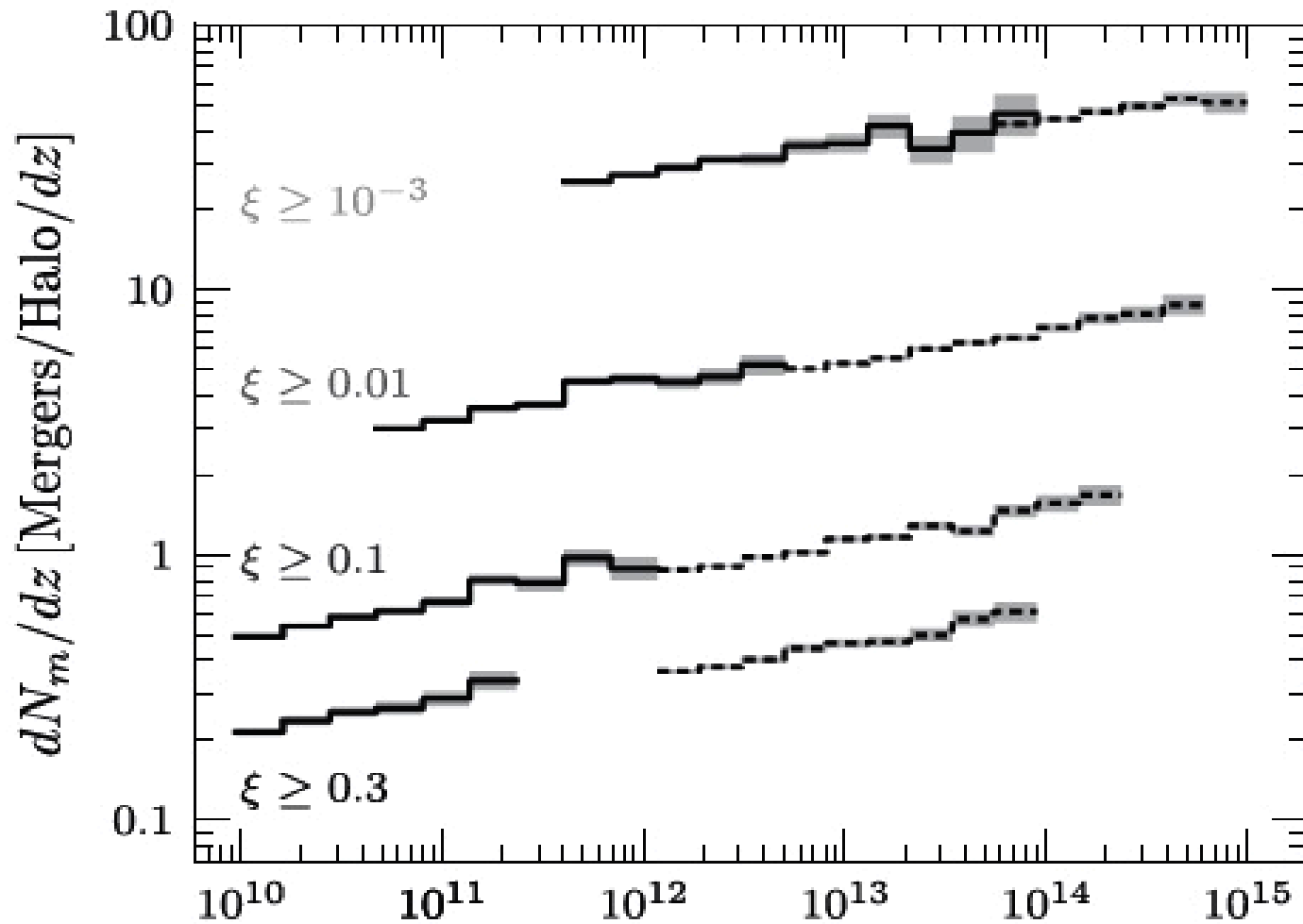
Number of mergers undergone by halos in the Millennium I and II simulations over history as a function of mass ratio M_i/M_1



Results arranged in bins of halo mass

Scaled by the number of halos in the simulation at the the present day.

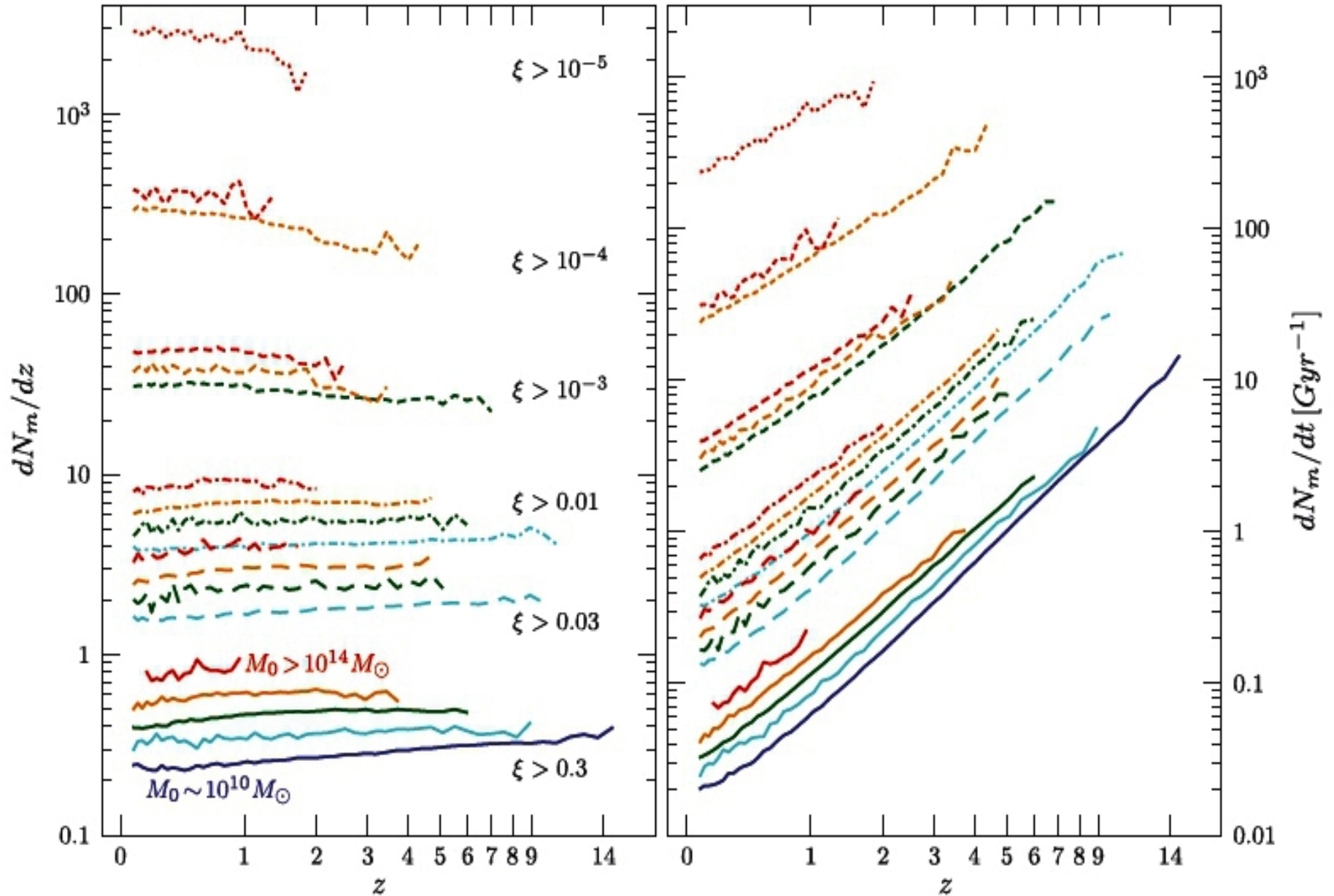
Halo mass dependence of the merging rate
is very weak.



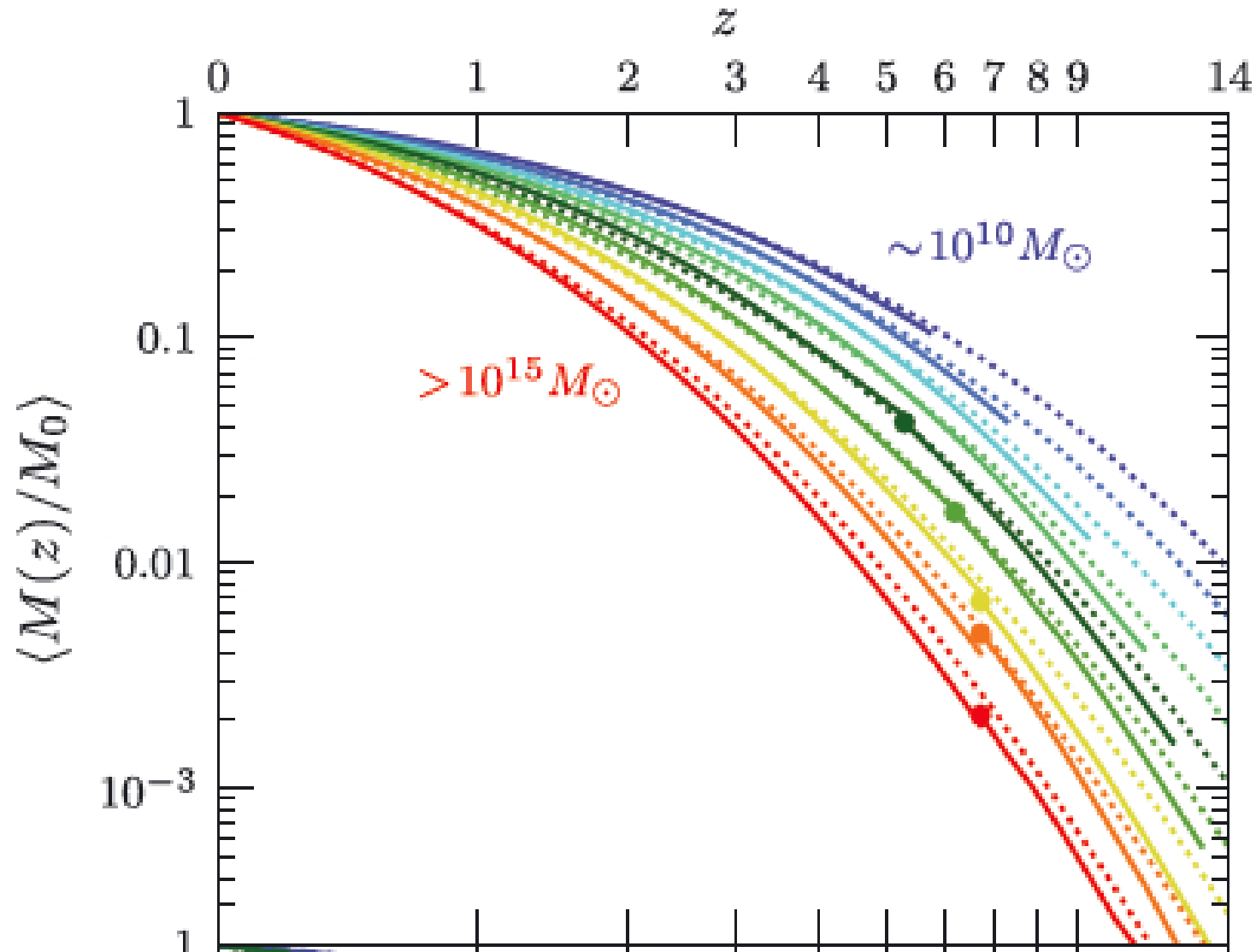
$$\frac{dN_m}{d\xi dz}(M, \xi, z) = A \left(\frac{M}{10^{12} M_\odot} \right)^\alpha \xi^\beta \exp \left[\left(\frac{\xi}{\tilde{\xi}} \right)^\gamma \right] (1+z)^\eta.$$

We find the best-fitting parameters to be $(\alpha, \beta, \gamma, \eta) = (0.133, -1.995, 0.263, 0.0993)$ and $(A, \tilde{\xi}) = (0.0104, 9.72 \times 10^{-3})$. The

Mass and redshift dependence of the merging rate

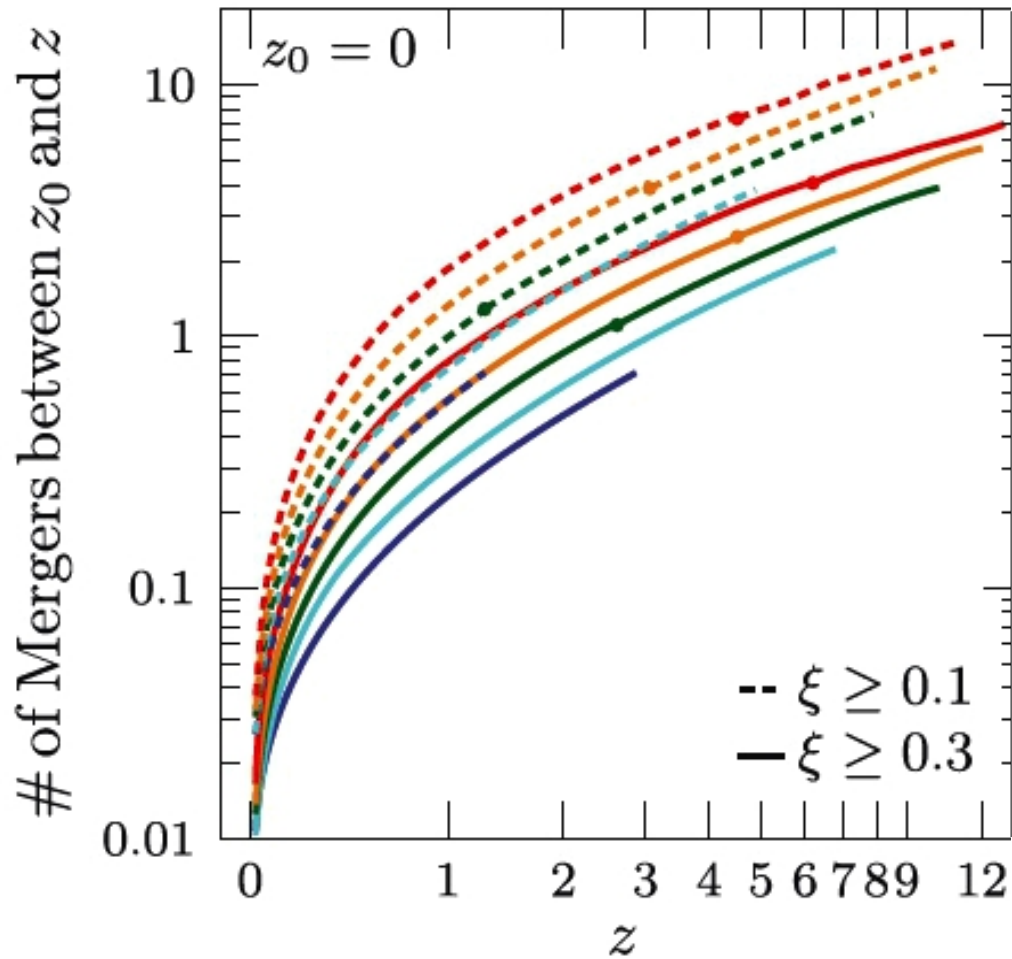


Mass growth of the largest progenitor as a function of z

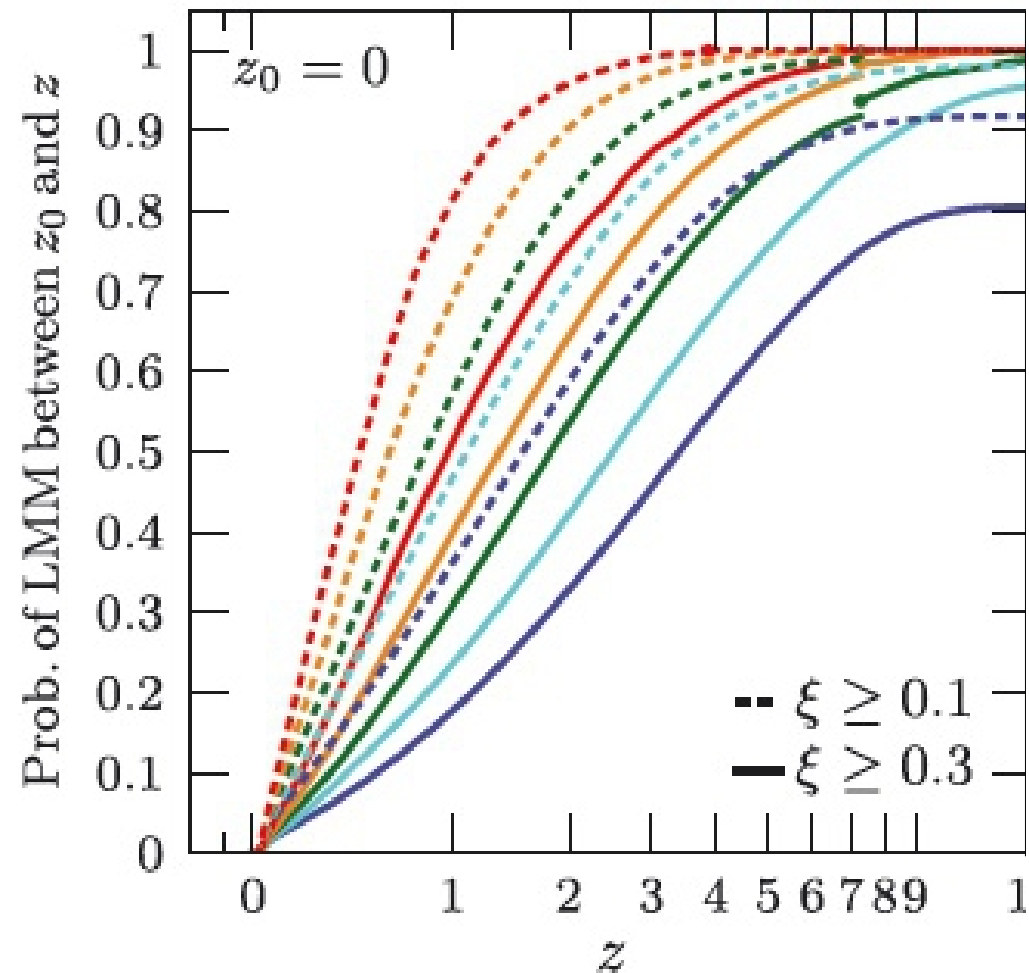


$$\langle \dot{M} \rangle_{\text{mean}} = 46.1 M_\odot \text{ yr}^{-1} \left(\frac{M}{10^{12} M_\odot} \right)^{1.1} \times (1 + 1.11z) \sqrt{\Omega_m (1+z)^3 + \Omega_\Lambda}$$

Cumulative number of mergers between redshift z and now

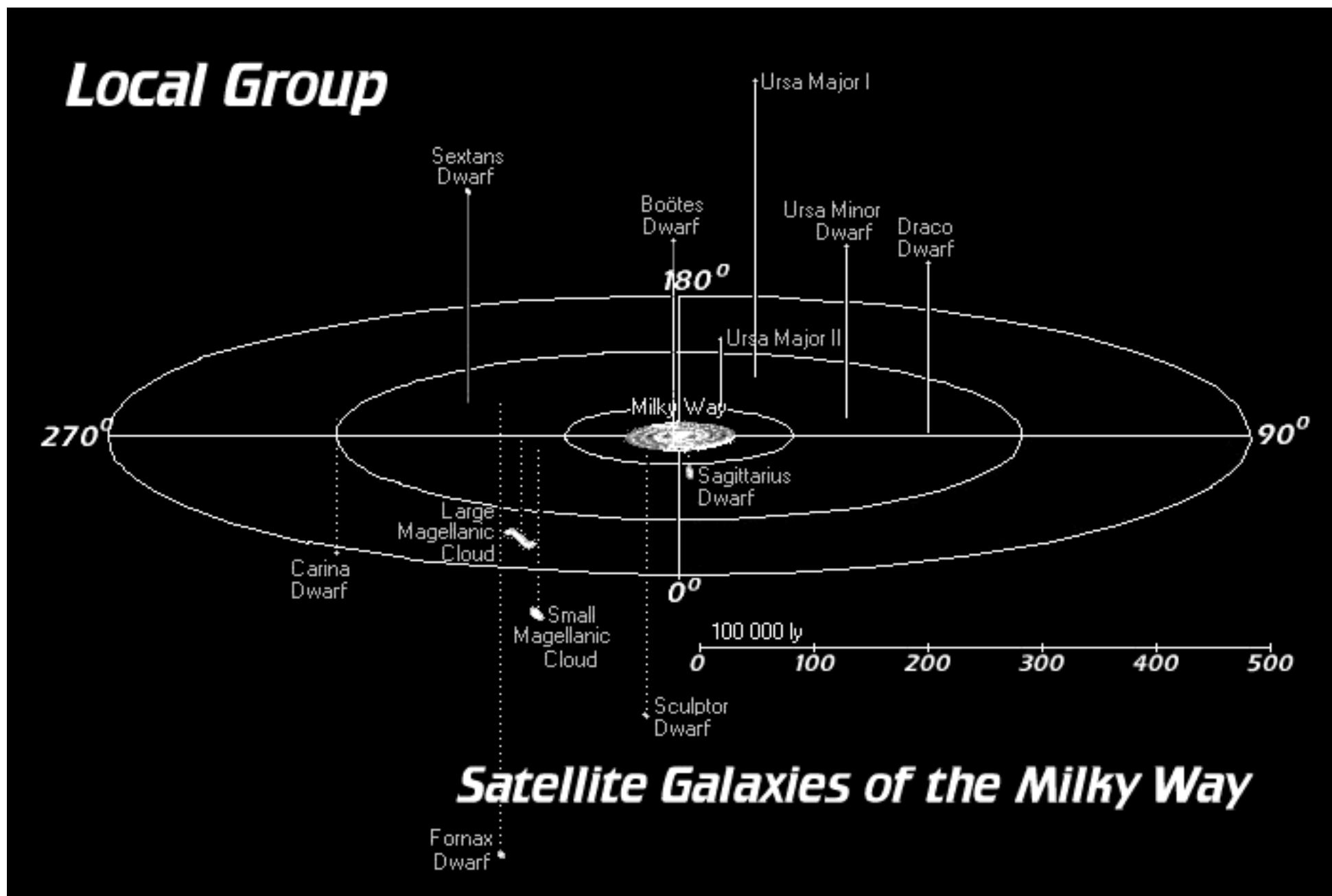


Probability of the last major merger having occurred between redshift z and now.

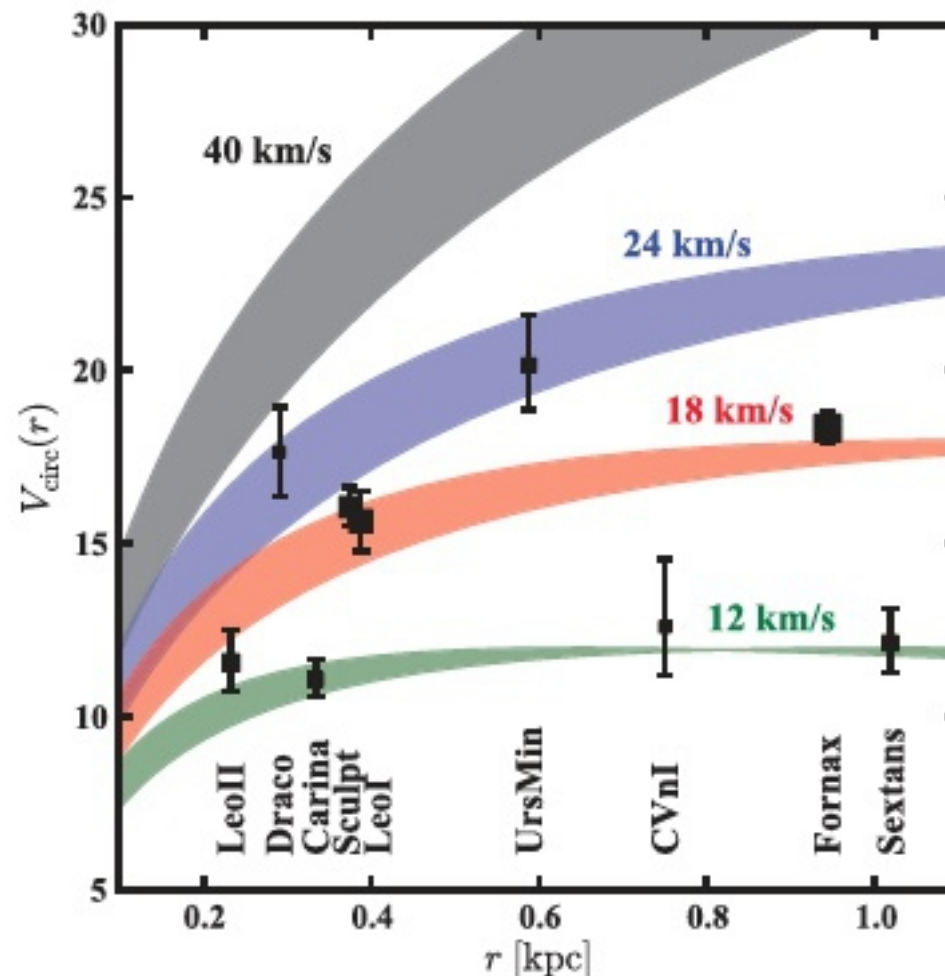


Massive halos are red, low mass halos are blue/purple.

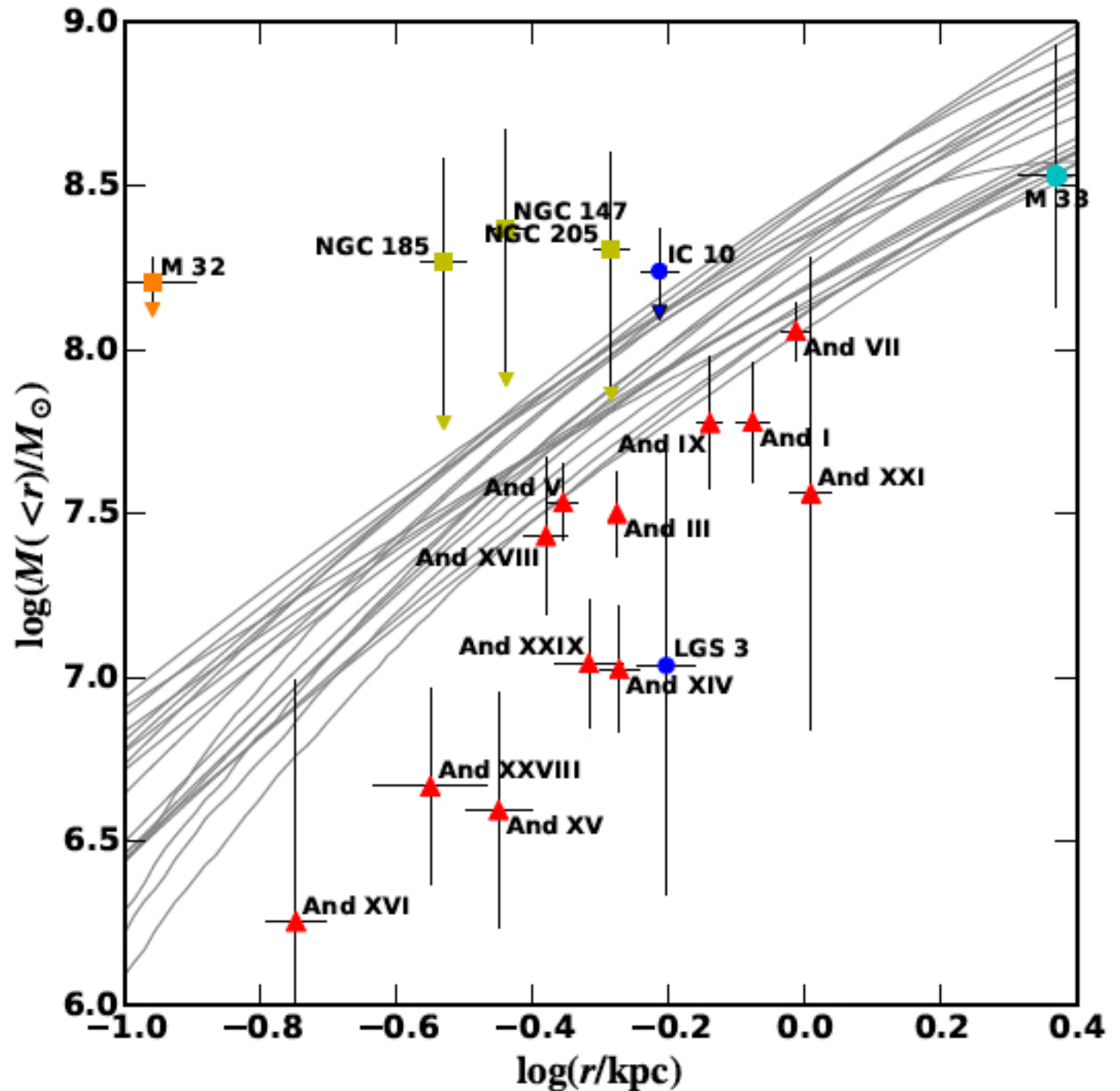
Observational Tests: Satellites of the Milky Way



We use the Aquarius simulations to show that the most massive subhaloes in galaxy-mass dark matter (DM) haloes in Λ cold dark matter (Λ CDM) are grossly inconsistent with the dynamics of the brightest Milky Way dwarf spheroidal galaxies. While the best-fitting hosts of the dwarf spheroidals all have $12 \lesssim V_{\text{max}} \lesssim 25 \text{ km s}^{-1}$, Λ CDM simulations predict at least 10 subhaloes with $V_{\text{max}} > 25 \text{ km s}^{-1}$. These subhaloes are also among the most massive at earlier times,



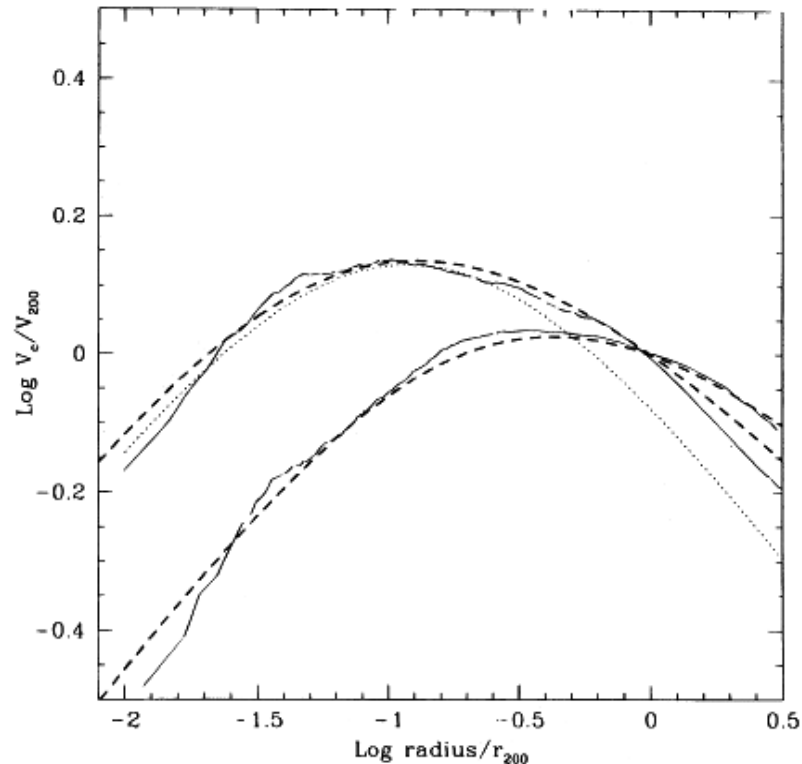
Same
problem for
M31



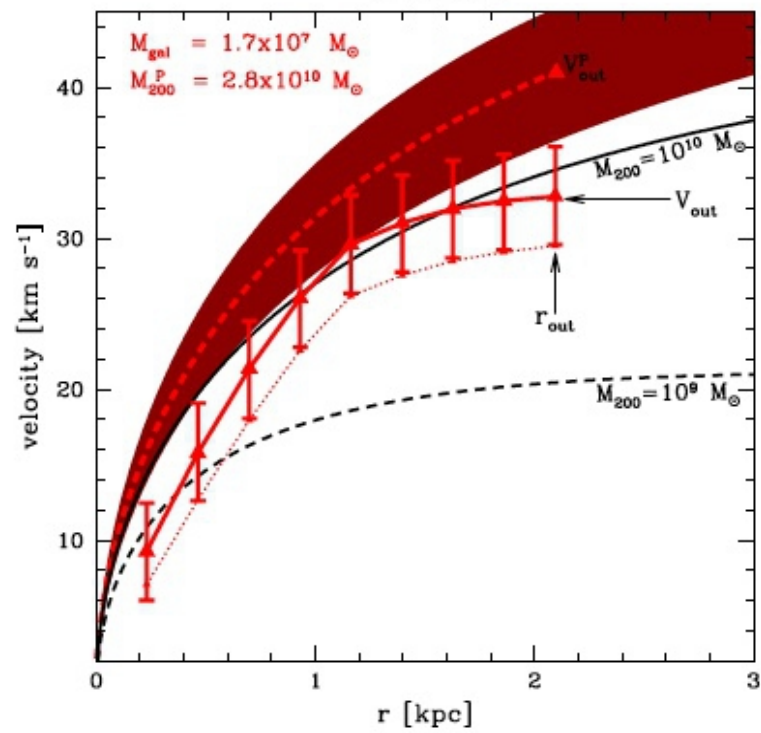
The NFW profile can be turned into a velocity profile using
 $V = (GM(r)/r^2)^{1/2}$

$$\left(\frac{V_c(r)}{V_{200}}\right)^2 = \frac{1}{x} \frac{\ln(1+cx) - (cx)/(1+cx)}{\ln(1+c) - c/(1+c)},$$

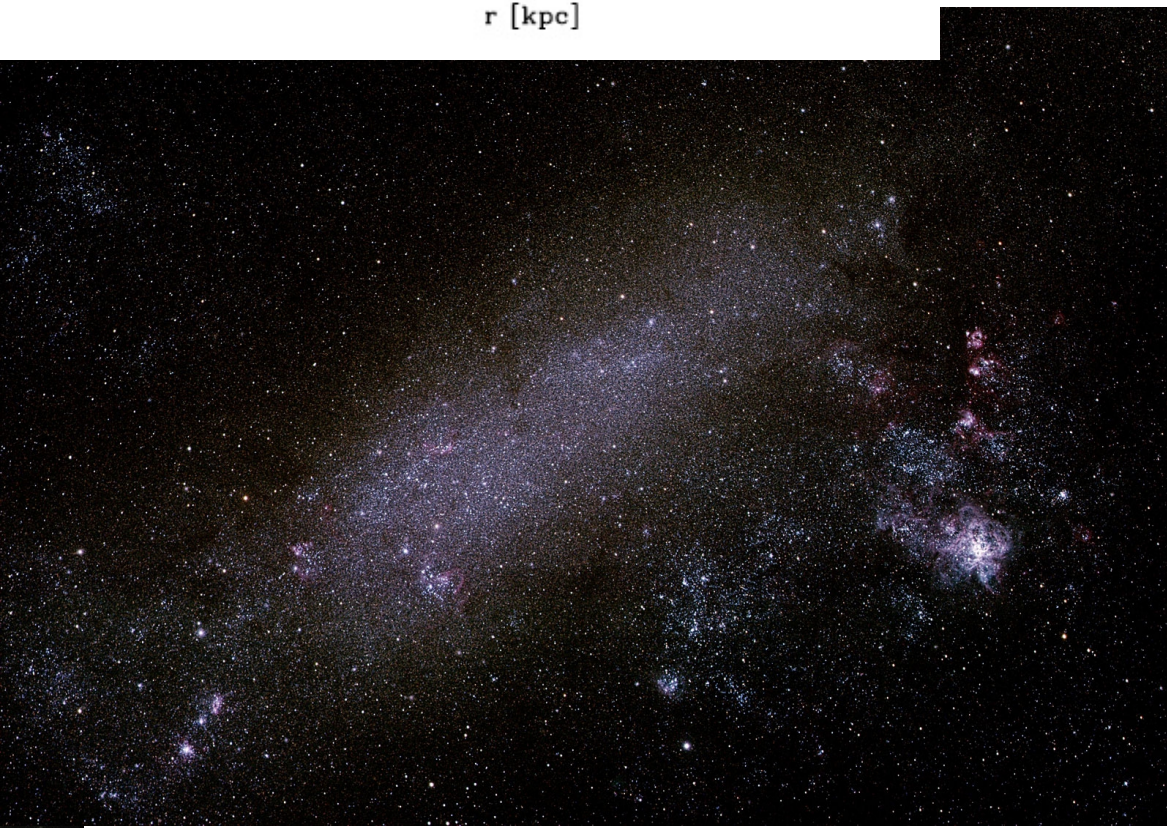
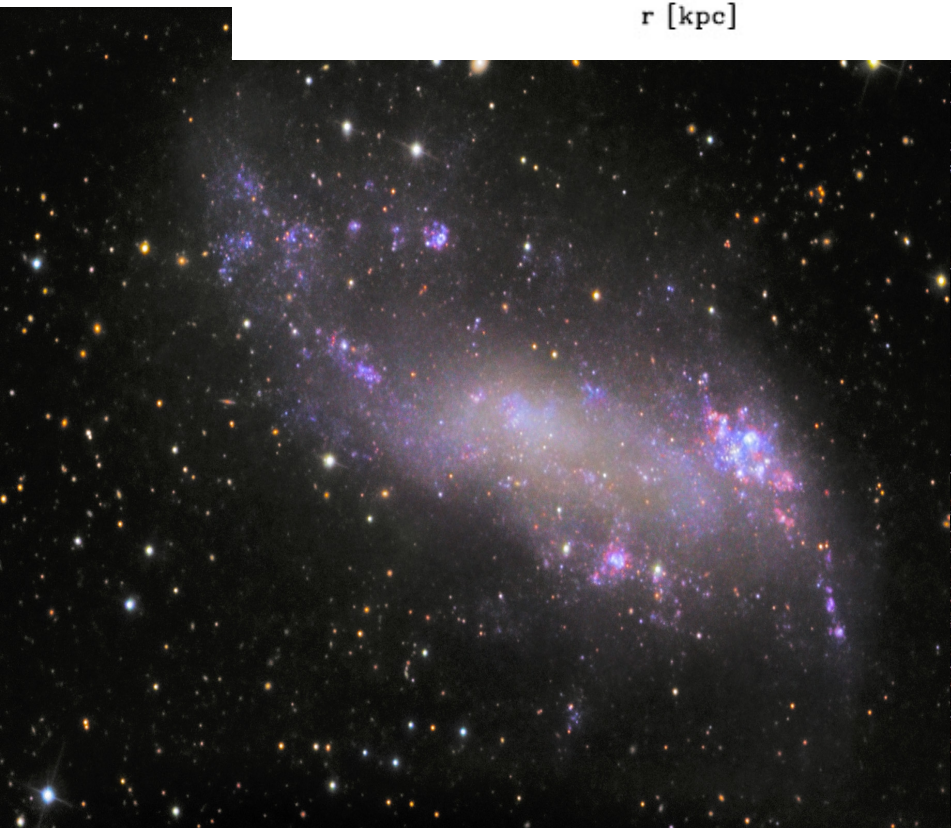
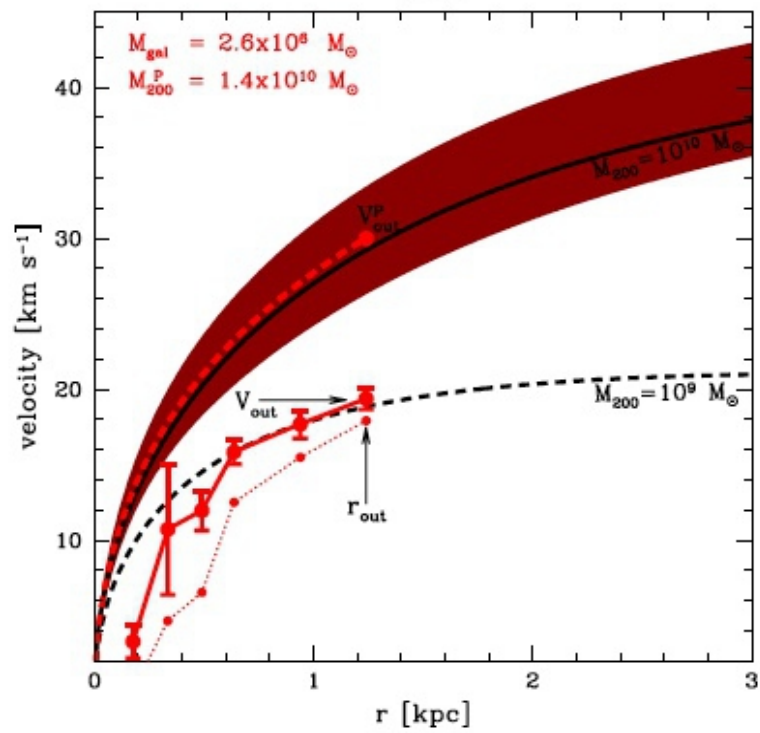
Where $x=r/r_{200}$ is the radius in units of the virial radius. Circular velocities rise near the center, reach a maximum (V_{\max}) at $x_{\max} \sim 2/c$, and decline near the virial radius. More centrally concentrated halos are characterized by higher values of V_{\max}/V_{200} .

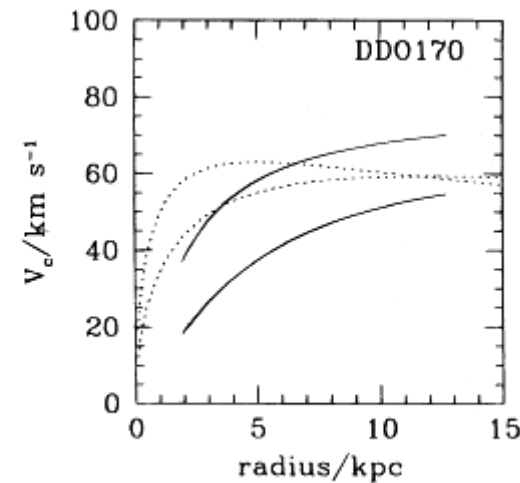
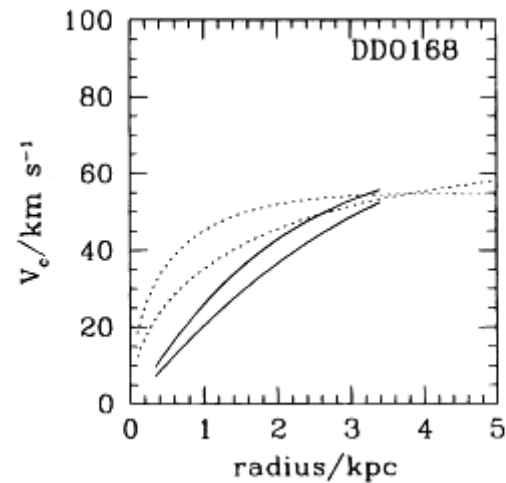
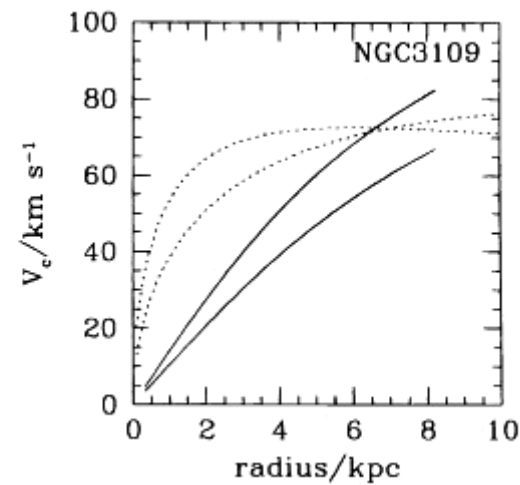
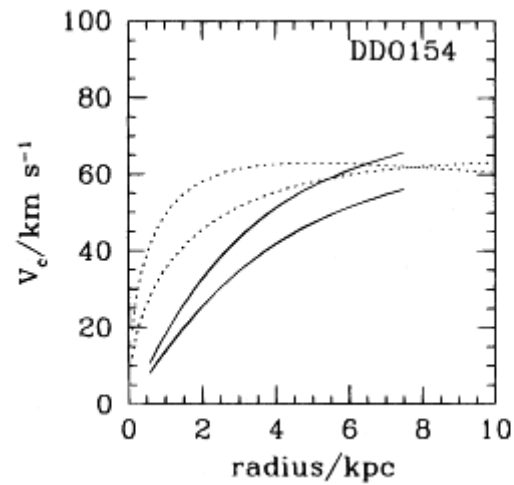


UGC 7559



SDIG





We conclude that, although the cores of dwarf galaxies pose a significant problem for CDM, the problem is not as bad as previously thought. Perturbations to the central regions of dwarf galaxy halos, resulting perhaps from the sudden loss of a large fraction of the baryonic material after a vigorous bout of star formation (Dekel & Silk 1986), can in principle reconcile the observations of dwarfs with the structure of CDM halos (Navarro, Eke, & Frenk 1995a).